INTERFACE

royalsocietypublishing.org/journal/rsif

Research

Cite this article: Fernandes MC, Saadat M, Cauchy-Dubois P, Inamura C, Sirota T, Milliron G, Haj-Hariri H, Bertoldi K, Weaver JC. 2021 Mechanical and hydrodynamic analyses of helical strake-like ridges in a glass sponge. *J. R. Soc. Interface* **18**: 20210559. https://doi.org/10.1098/rsif.2021.0559

Received: 3 July 2021
Accepted: 16 August 2021

Subject Category:
Life Sciences–Engineering interface

Subject Areas:
biomaterials, evolution, biomechanics

Keywords:
vortex shedding, strakes, ribs, bioinspired, *Euplectella aspergillum*, ridges

Author for correspondence:
James C. Weaver
e-mail: jweaver@seas.harvard.edu

Electronic supplementary material is available online at https://doi.org/10.6084/m9.figshare.c.5581086.

THE ROYAL SOCIETY PUBLISHING

Mechanical and hydrodynamic analyses of helical strake-like ridges in a glass sponge

Matheus C. Fernandes[1,2], Mehdi Saadat[3], Patrick Cauchy-Dubois[1], Chikara Inamura[4], Ted Sirota[1,2], Garrett Milliron[5], Hossein Haj-Hariri[6], Katia Bertoldi[1,2] and James C. Weaver[1,2]

[1]John A. Paulson School of Engineering and Applied Sciences, [2]Wyss Institute for Biologically Inspired Engineering, and [3]Department of Organismic and Evolutionary Biology, Harvard University, Cambridge, MA 02138, USA
[4]Media Lab, Massachusetts Institute of Technology, Cambridge, MA 02139, USA
[5]Collective Design, Grand Rapids, MI 49505, USA
[6]College of Engineering and Computing, University of South Carolina, Columbia, SC 29208, USA

MCF, 0000-0002-6252-9300; JCW, 0000-0002-6522-7359

From the discovery of functionally graded laminated composites, to near-structurally optimized diagonally reinforced square lattice structures, the skeletal system of the predominantly deep-sea sponge *Euplectella aspergillum* has continued to inspire biologists, materials scientists and mechanical engineers. Building on these previous efforts, in the present study, we develop an integrated finite element and fluid dynamics approach for investigating structure–function relationships in the complex maze-like organization of helical ridges that surround the main skeletal tube of this species. From these investigations, we discover that not only do these ridges provide additional mechanical reinforcement, but perhaps more significantly, provide a critical hydrodynamic benefit by effectively suppressing von Kármán vortex shedding and reducing lift forcing fluctuations over a wide range of biologically relevant flow regimes. By comparing the disordered sponge ridge geometry to other more symmetrical strake-based vortex suppression systems commonly employed in infrastructure applications ranging from antennas to underwater gas and oil pipelines, we find that the unique maze-like ridge organization of *E. aspergillum* can completely suppress vortex shedding rather than delaying their shedding to a more downstream location, thus highlighting their potential benefit in these engineering contexts.

1. Introduction

The geometrically complex siliceous skeletal systems of marine sponges have attracted a great deal of attention from the scientific community due to their multi-scale structural hierarchical organization and remarkable damage tolerance [1–3]. For example, the mineralized tubular skeleton from one such species, *Euplectella aspergillum*, consists of bundles of individual needle-like elements (spicules) that are cemented together to form a diagonally reinforced square lattice-like structure that is further covered by a series of helical ridge-like features [4,5]. Detailed investigations into the various components of this structural hierarchy have revealed their surprising mechanical benefits.

First, single-spicule studies have revealed the presence of an underlying laminated architecture consisting of concentric lamellae of consolidated silica nanoparticles separated by thin organic interlayers. The silica layers decrease in thickness from the spicule core to its periphery, resulting in a functionally graded design that effectively retards crack propagation through the spicules, while simultaneously increasing their buckling resistance [3,6].

At a second level of structural hierarchy, bundles of these laminated spicules are further organized into a square lattice-like structure which is reinforced by pairs of diagonal struts that cross through every other cell of the lattice, creating a checkerboard-like organization. Through a combination of finite element (FE) simulations and direct mechanical testing, it has been demonstrated

that this non-intuitive diagonal reinforcement strategy creates a geometry that exhibits a near-optimal strength-to-weight ratio for this specific family of truss structures [7].

Finally, surrounding the underlying diagonally reinforced square lattice are a series of right- and left-handed helical ridges, which are oriented perpendicular to the surface of the skeletal tube and form a distinctive maze-like organization. While previous studies have speculated that these ridge-like features provided a mechanical benefit to the sponge [4], as has been demonstrated for other reinforcing axial and helical rib-like elements on tubular structures [8–10], the striking morphological similarity of the sponge ridges to helical strakes used for vortex suppression in cylindrical structures under flow [11–14] motivated the present study which explores their potential hydrodynamic functionality.

Vortex shedding is a topic of great concern to the engineering community, not only for its ability to excite vortex-induced vibrations, potentially leading to resonance structural vibrations [12,15], but also for its periodic forcing effects and noise generation [11]. Fluid flow past bluff cylindrical structures is known to generate vorticity due to the presence of shear in the fluid's boundary layer. These small vorticity regions coalesce into regions of concentrated vorticity on both sides of the cylinder, leading to a phenomenon known as von Kármán vortex shedding. [12] Because of the implications of von Kármán vortex shedding on the structural integrity of cylindrical forms, the addition of helical strakes (protruding ridge-like elements) is commonly employed as a method to suppress this effect [11,13].

Here, we describe a computational framework for investigating structure–function relationships of the complex helical ridge system in the skeleton of *Euplectella aspergillum*. Using an integrated approach that combines FE simulations and computational fluid dynamics, we explore both the mechanical and hydrodynamic effects of these skeletal features and compare these results to alternative ridge geometries employed for similar functions in their synthetic engineering analogues.

2. Skeletal geometry

As demonstrated from previous studies [4], the skeletal system of a fully mature specimen of *E. aspergillum* (figure 1*a*) is covered with a laminated silica cement, forming a rigid construct, and contains a maze-like network of external helical ridges that extend perpendicular to the skeletal tube. To explore the organizational details of this complex ridge system, we examined ten different sponge skeletal samples and manually mapped each of the different ridge designs, ultimately constructing a series of planar ridge connectivity diagrams, a representative example of which is shown in figure 1*b* (all 10 maps are shown in electronic supplementary material, figure S1). In this surface map (which corresponds to the upper *ca* 50% of the skeleton where the ridges are most pronounced and easily identified), the coloured squares represent the ridge locations (the ridge-less unit cells are white), with red squares denoting clockwise ridges and blue squares denoting counterclockwise ridges (corner elements are denoted in purple). From examination of these different sponge specimens, we identified several common ridge design themes, which include the following (and are consistent with observations from previous studies [4]):

— The ridges occur at 45° angles relative to the long axis of the skeletal tube.
— The ridges populate, on average, every other closed square in the skeletal lattice.
— The ridges intersect at 90° angles.
— The ridges never cross each other; however, they may form T-junctions.
— The total number of ridge-filled cells is similar between specimens, as shown by the purple bar in figure 1*c*, which denotes the mean ridge quantity for 10 different sponge specimens (error bars represent ±1 s.d.).
— The total number of clockwise ridges is similar to that of the total number of counterclockwise ridges, as denoted by the red and blue bars in figure 1*c*, which correspond to the mean clockwise and counterclockwise ridge lengths for 10 different sponge specimens (error bars represent ±1 s.d.).

Finally, it is important to note that, on average, the height of the ridges linearly increases from *ca* 1 mm to *ca* 6 mm from its anchoring point on the seafloor to its apex (illustrated by the green line in figure 1*d*) [4]. Despite this increasing ridge height, a relatively constant material volume per unit area has been measured along the length of the tapered skeletal network (illustrated by the dotted black line in figure 1*d*) [4], which results from a simultaneous increase in lattice unit cell size and a relatively constant strut thickness, which lead to a corresponding decreasing strut width-to-unit cell width ratio as one ascends the sponge (illustrated by the orange line in figure 1*d*).

3. Model generation

To construct the three-dimensional models (described in detail in figures 2–4) used in both our mechanical and hydrodynamic studies, we subdivided the geometry into two primary components: (1) the hollow cylindrical core and (2) the external ridge system.

3.1. Hollow cylindrical core

3.1.1. Structural analysis

For the structural analyses, we considered only the load-bearing glassy skeletal components of the sponge. To produce this model, we tiled the diagonally reinforced square lattice geometry described in Fernandes *et al.* [7] (figure 2*a*) to generate a tubular lattice (figure 2*b*), which consisted of 32 horizontal struts, and 32 vertical struts in circumference (creating a cylinder with a height to radius ratio $H/R \sim 6.2$). The ratio between the strut diameter and strut separation was $D_{nd}/L = 0.1$ (where L is the square grid strut separation) to match the average dimensions found in this species [7] (figure 2*a*). Overlaid on this square grid is a system of paired diagonal reinforcing struts (figure 2*a*), the periodic spacing of which creates a checkerboard-like open and closed cell structure, where every open cell contains an octagonal aperture. This geometry leads to two independent pairs of crisscrossing diagonals struts, each with a spacing of

$$S = \frac{L}{\sqrt{2}+2}. \tag{3.1}$$

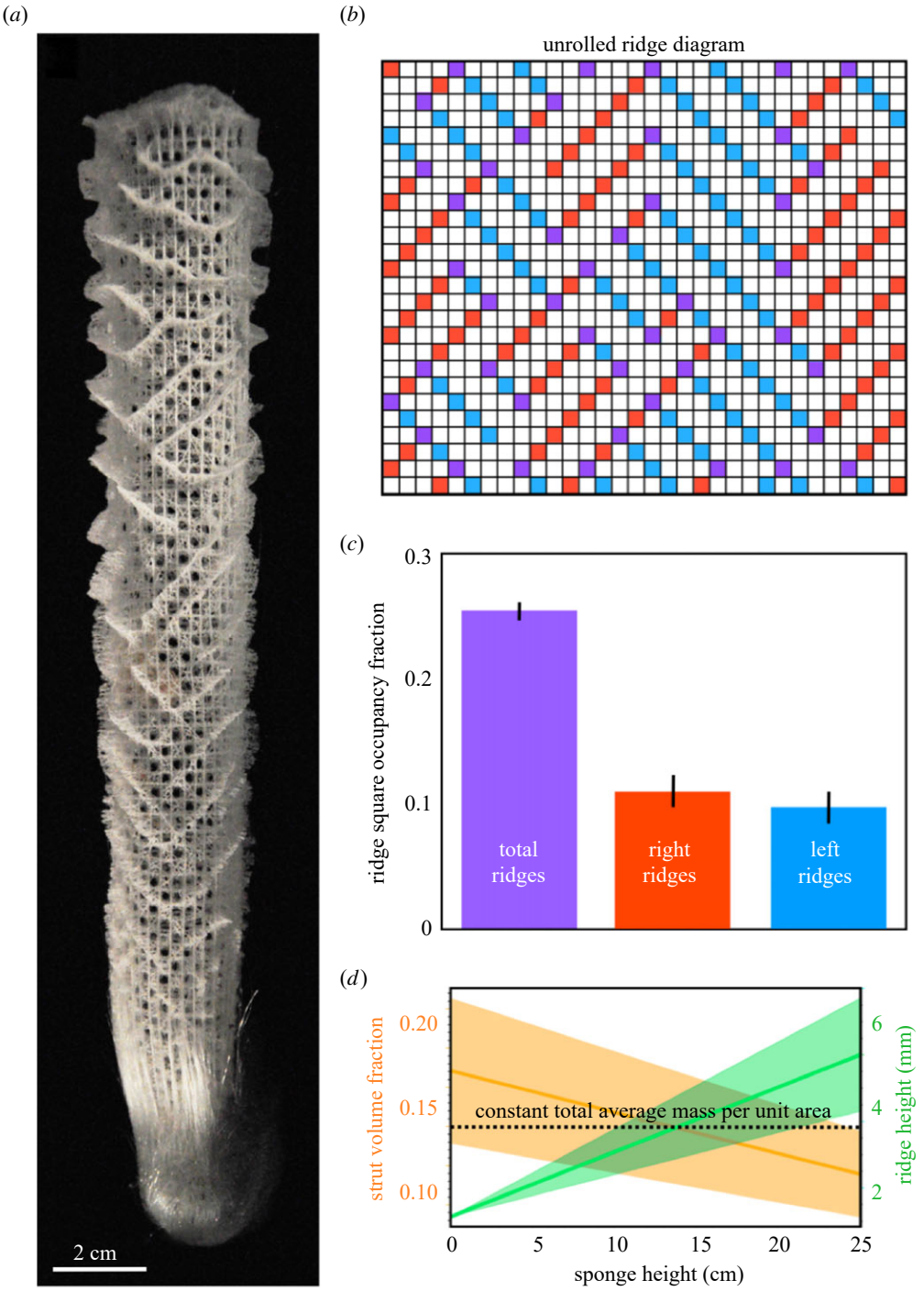

Figure 1. Skeletal features of *Euplectella aspergillum*. (*a*) Photograph of a cleaned and dried siliceous skeleton of *E. aspergillum* (measuring *ca* 25 cm in height) clearly depicting its tapered tubular form, its highly regular diagonally reinforced checkerboard-like square lattice structure, and its complex network of external ridges. (*b*) Unrolled ridge diagram illustrating the location of ridge elements in relation to the checkerboard-like lattice system. Filled squares denote the presence, and white squares denote the absence of ridge elements. Red squares denote clockwise ridge elements, blue squares denote counterclockwise ridge elements and purple squares denote corner elements (which do not count toward the number of either clockwise or counterclockwise elements). (*c*) Bar plot showing the mean occupancy fraction for ridge elements ($n = 10$ from electronic supplementary material, figure S1). Data presented are averages, and error bars represent ±1 s.d. The purple bar shows the total ridge occupancy fraction, which includes all clockwise (red bar), counterclockwise (blue bar) and corner elements. (*d*) Plot adapted from Weaver *et al.* [4], which illustrates that the combination of a decreasing volume per unit area for the underlying diagonally reinforced square lattice (orange) with an increasing ridge height (green) along the length of the tapered tube, results in a relatively consistent total material volume of silica per unit area throughout the entire skeletal system (black dotted line). For the orange and green data, the solid lines denote averages and the shaded regions denote ± 1 s.d. for $n = 10$ specimens.

In this configuration, the pairs of diagonals are thinner than the non-diagonal struts [4,7], with a relationship given by [7]

$$D_d = \frac{D_{nd}}{2}. \tag{3.2}$$

Numerical values of these parameters used in our simulations can be found in electronic supplementary material, table S1.

3.1.2. Hydrodynamic analysis

For the hydrodynamic analyses, we explored three different geometries for the cylindrical core, all characterized by an external radius R_o, an internal radius $R_i = 0.9R_o$ and a height $H = 6.2R_o$.

— *No Pores*: This design consisted of a featureless smooth cylinder (see figure 3, second column), a geometry that

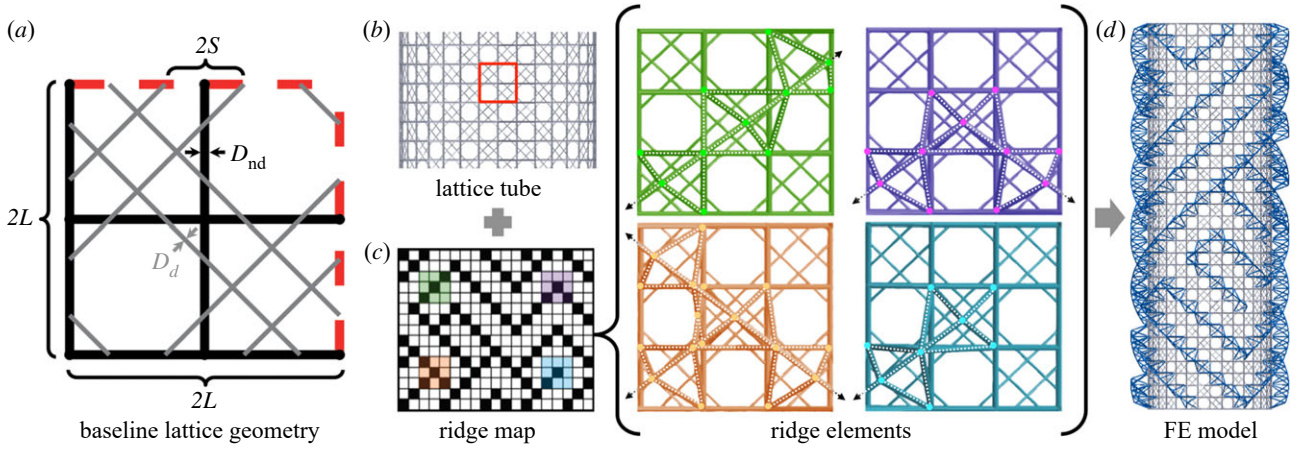

Figure 2. Workflow for the generation of sponge structural models. (*a*) Schematics showing the underlying diagonally reinforced square unit-cell geometry, which was tiled to produce the tubular lattice shown in (*b*). (*c*) Schematics showing the different ridge elements used to construct the complete skeletal model. Each component is colour-coded in the left map, indicating its location. The dotted lines in each of the four three-dimensional models correspond to the main ridge supporting elements, the brightly coloured dots denote nodes of fusion between the struts, and the black arrows denote the direction of ridge elongation. To construct the complete ridge system for each tested sponge geometry (as shown in (*d*)), each of these four elements could be either translated, rotated or mirrored (with the exception of the *Bidirecitonal* design which requires an additional crossing element).

has been widely studied in the field of hydrodynamics, and is known to produce von Kármán vortices [16,17].

— *Small Pores*: Inspired by the anatomy of living specimens of *E. aspergillum*, small holes (approximated as octagons) populate locations corresponding to the positions of every open square in the underlying diagonally reinforced skeletal lattice (figure 3, third column). In this configuration, the effective surface porosity is given by $\phi_s = 0.06$. For details regarding the geometry and porosity calculations, see electronic supplementary material, figure S2.

— *Large Pores*: This geometry is very similar to that of the *Small Pores* tube, but with larger diameter holes (figure 3, fourth column). The porosity of this design approximates that of only the sponge's skeleton, and the effective surface porosity of this structure is given by $\phi_s = 0.41$. While this specific geometry is not directly relevant to the living sponge, it provides a useful experimental test bed for investigating the effect of pore fraction on hydrodynamic performance. For the details regarding geometry and porosity calculations, see electronic supplementary material, figure S2.

To create the small and large pore models, respectively, octagonal openings measuring with side $S_0 = 0.16L$ (figure 4*f*,*g*) and $S_0 = 0.4L$ (figure 4*h*,*i*) were cut through the cylinder-ridge construct.

3.2. External ridge system

For our structural and hydrodynamic analyses, we considered three different diagonal ridge arrangements (figure 3).

— *Unidirectional Ridges*: This geometry consists of eight uninterrupted parallel *unidirectional* helical ridges, each of which measures 32 cells in length, and occupy every other filled square cell of the sponge's skeletal lattice (figure 3*b*).

— *Bidirectional Ridges*: As with the unidirectional ridge model, this design also incorporates eight helical ridges, each of which measures 32 cells in length. However, for this design, four of the helices are right-handed and four are left-handed (figure 3*c*).

— *Sponge Ridges*: Inspired by the external ridge structure of *E. aspergillum*, this geometry is composed of a maze-like combination of right- and left-handed ridges that occupy every other filled square cell of the sponge's skeletal lattice. One example (from the list of 10 mapped sponges) is shown in figure 3*d*. The other nine mapped designs can be found in electronic supplementary material, figure S1.

It is important to note that for the three different ridge configurations described above, the total ridge lengths are nearly identical. Furthermore, in all our models, we chose the height of the ridges to be $h_r = 1.45L$, which is equivalent to the mean ridge height (R_r–R_o in figure 4*c*,*d*) across the length of the sponge [4].

3.2.1. Structural analyses

To generate the ridges for our structural models, we first identified the four distinctive design elements shown in figure 2*c*, which formed the basis of a complete ridge system. These elements are a result of ridge continuations (green schematic), 90° turns (purple schematic), T-junctions (orange schematic) and ridge terminations (blue schematic) in the sponge ridge system. Utilizing these elements and their possible rotations, we generated all of the different ridge-containing models. For all of the struts composing the ridge structure, the diameter matched that of the non-diagonals, namely, $D_{rg} = D_{nd}$, where D_{rg} is the ridge strut diameter and D_{nd} is the non-diagonal strut diameter.

3.2.2. Hydrodynamic analysis

To generate the ridges for our hydrodynamic models (which were modelled after those found in living examples of *E. aspergillum*), we began with a planar ridge diagram (figure 4*a*), which was used as a road map to construct a series of triangular surface ridges (figure 4*b*) on an extruded 32-sided polygon (which approximated the cylindrical geometry of the sponge). The flat-sided ridges were designed such that their apex ran diagonally through the squares in the planar ridge map, and contacted the cylinder at a location that corresponded to the geometric centres of each of the

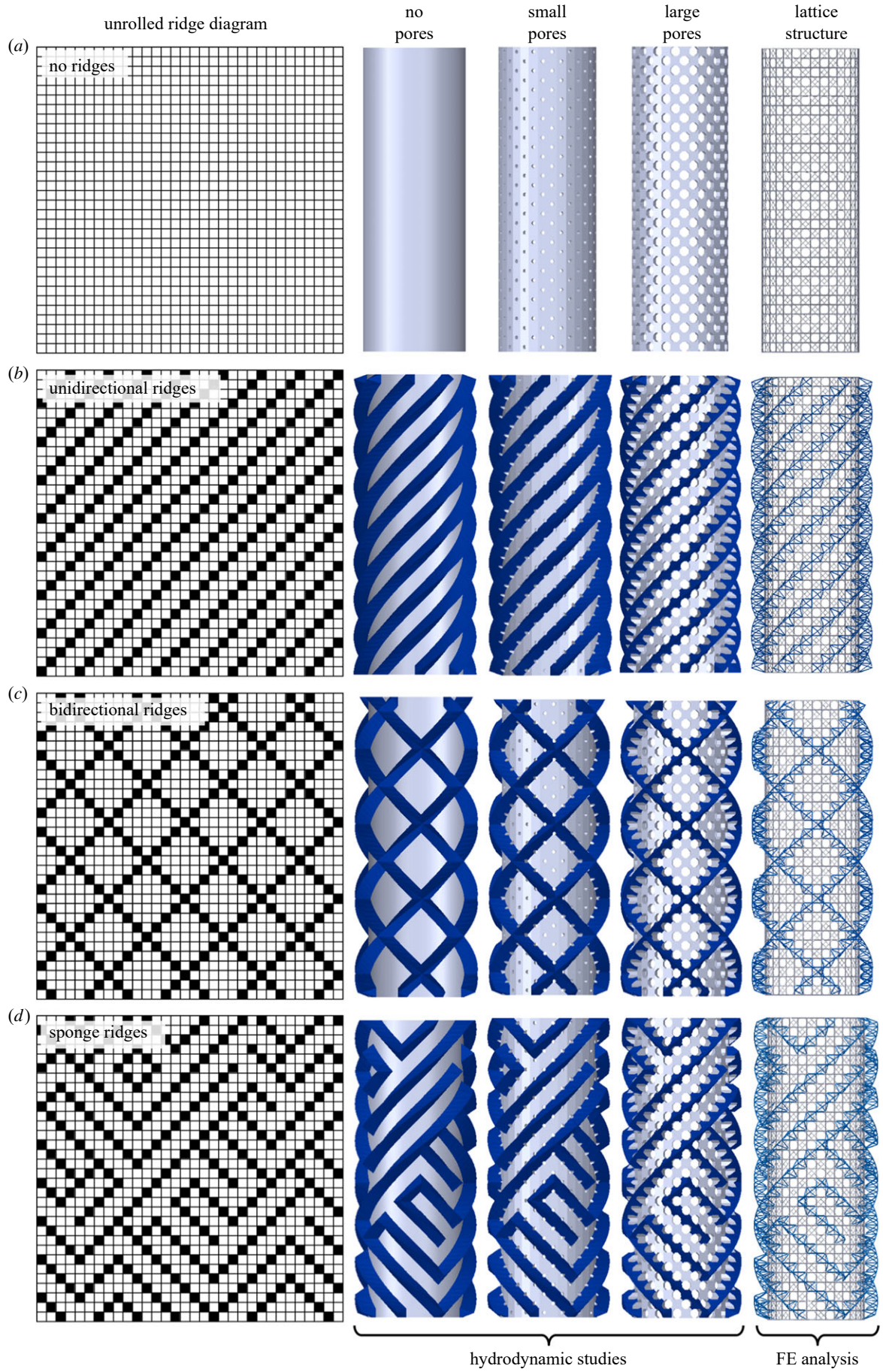

Figure 3. Fully constructed models for structural and hydrodynamic analyses. Schematics showing (*a*) the ridge-free baseline cylinder, (*b*) the *Unidirectional* ridge design, (*c*) the *Bidirectional* ridge design and (*d*) one representative example of the *Sponge* ridge design. For each ridge geometry, we also considered four variations of the inner tube (left to right): a solid (non-porous) tube, a low-porosity tube (approximating the porosity of the living sponge), a high-porosity tube (approximating the porosity of only the skeleton), and that of only the load-bearing skeletal elements of a sponge. CFD simulations were conducted on the first three tube geometries (solid, low-porosity and high-porosity geometries) and FE simulations were conducted on the last geometry (load-bearing skeletal elements).

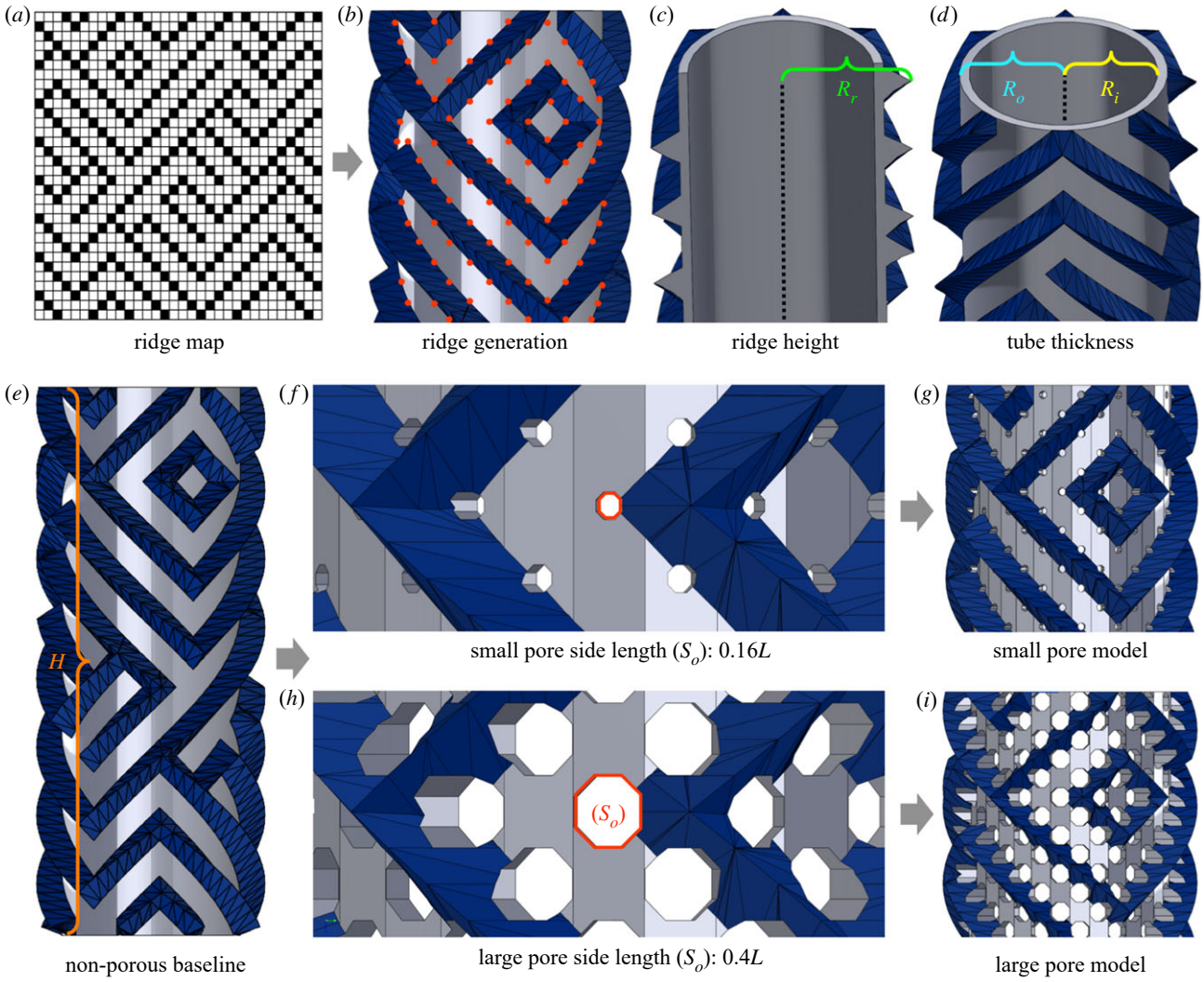

Figure 4. Hydrodynamic model generation workflow. (*a*) Schematic showing one of the ten sponge ridge diagrams that provided a road map for construction of a complete ridge network. (*b*) The apex of the triangular ridges (blue) cross diagonally through the black squares in (*a*) and their flat sides contact the underlying cylinder (grey) at the geometric centres (denoted by red dots) of the octagonal openings shown in figure 2*a*. (*c*) Schematic showing a cross-sectional view of the non-porous cylindrical core (grey) with the labelled radius encompassing the ridge height R_r. (*d*) Schematic showing the cylinder thickness parameters, with R_o and R_i denoting the outer and inner radii, respectively. For (*c*,*d*), the vertical black dotted lines denote the model's neutral axis. (*e*) Schematic showing the complete non-porous baseline ridge geometry (with the model height, *H*, specified), which was generated from the sponge ridge diagram shown in (*a*). High (*f*) and low (*g*) magnification views, showing the geometries of the octagonal holes (red) for the *Small Pores* model containing a side length of $S_o \approx 0.16L$, which approximates the porosity of a living sponge. High (*h*) and low (*i*) magnification views, showing the geometries of the octagonal holes (red) for the *Large Pores* model containing a side length of $S_o \approx 0.4L$, which approximates the porosity of only the sponge's glassy skeletal system.

octagonal openings shown in figure 4*a* (and denoted by the red dots in figure 4*b*). It is important to note that while the underlying skeletal geometry of the ridges is incredibly complex (as shown in figure 2), in the living sponge, the organic material conceals much of this underlying structural complexity, and thus only approximates the rough contours of the underlying skeletal system [18–20], thus permitting the construction of the simpler (and still biologically relevant) ridge geometry shown in figure 4.

4. Structural analyses

4.1. Methods

In an effort to understand how the ridges affected the sponge's structural performance, we conducted FE simulations using ABAQUS/Standard (Dassault Systémes SE). For these analyses, the geometries were constructed using Timoshenko beam elements (ABAQUS element-type B22) with circular cross-sections and the material's response was captured using a linear elastic material model with Young's modulus E_{mat}. In our simulations, we considered the ten different sponge ridge designs shown in electronic supplementary material, figure S1, and compared their response to the *Unidirectional* and *Bidirectional* models. We also considered a model without ridges, where the ridge material was instead allocated to the cylindrical beams of the underlying diagonally reinforced square lattice (we refer to this model as the *Reallocated Ridge Mass* model).

For each design, we assumed that the cylindrical sponge structure was fully constrained at its base (i.e. $u_x = u_y = u_z = 0$), and performed two different analyses: (1) a linear static analysis to extract the stiffness and (2) a buckling analysis (*BUCKLE step in ABAQUS) to obtain the critical buckling force. In the simulations, we considered four loading cases (illustrated in figure 5*a*).

— *Compression*: For this case, we applied a vertical displacement parallel to the *z*-axis ($\delta_{appl} = \delta_z$) to all the nodes of the top ring.
— *Torsion*: For this case, we applied a tangential displacement ($\delta_{appl} = \delta_\theta = \theta_{appl} R$) to all the nodes of the top ring.

— *Bending*: For this case, we applied a displacement in the x–y plane ($\delta_{\text{appl}} = \sqrt{\delta_x^2 + \delta_y^2}$) to all the nodes of the top ring. Note that we systematically varied δ_x and δ_y to survey the bending behaviour in different directions. Specifically, we considered eight equally spaced loading directions for each structure.
— *Pressure*: For this case, we applied a radial displacement ($\delta_{\text{appl}} = \delta_R$) to all nodes belonging to the cylindrical core of the models.

To implement these boundary conditions for *Compression*, *Torsion* and *Bending*, we constrained the degrees of freedom of the nodes of the top ring to a virtual node using equation constraints. Similarly, for the loading case *Pressure*, we tied the degrees of freedom of all nodes belonging to the cylindrical core to a virtual node using equation constraints. For all loading cases, we then applied δ_{appl} to the virtual nodes and extracted the resulting reaction force RF.

4.2. Results

In figure 5*b*,*c*, we report the numerically predicted stiffness and critical buckling load for all considered models and loading cases. We find that the addition of ridges increases the overall stiffness of the cylindrical structure for loading conditions *Bending* and *Pressure* (figure 5*b*) and improves the buckling performance for all loading conditions on average by *ca* twofold over the ridge-free example (figure 5*c*). However, if we compare the performance between the different ridge-containing geometries, we see that the stiffness values differ negligibly between the different ridge designs. By contrast, if the ridge material volume was instead allocated away from the ridge system and into the main cylindrical truss frame, the resulting structure, on average, measurably outperforms the other designs for most loading conditions in terms of both stiffness and buckling force. This result is not unexpected, since in this scenario, more material is allocated to the truss members aligned parallel to the loading direction.

These results demonstrate that the unusual maze-like ridge pattern found in *E. aspergillum* does not likely add any significant additional mechanical benefit (with regards to either stiffness or critical buckling force) compared to the other investigated ridge geometries, which prompted additional studies into its potential hydrodynamic functions (see §5). Further, the observation that reallocating the ridge material into the underlying diagonally reinforced skeletal lattice resulted in a significant enhancement in the structure's mechanical performance may be functionally relevant to the sponge's skeletal anatomy. As shown in figure 1*d*, the sponge's material volume per unit area remains relatively constant along the length of the tapered skeletal tube, which is achieved due to an increase in ridge height (and volume), from the base of the sponge to its apex, and a corresponding loss in volumetric skeletal density of the underlying diagonally reinforced square lattice (which results from an increase in vertical and horizontal strut spacing). As such, the mechanically most robust portion of the composite skeleton coincides with its thickened and ridgeless connection point to the flexible holdfast apparatus, which secures the sponges into the soft sediments of the sea floor. Based on our results, this transition in the skeletal anatomy from the rigid skeleton to its flexible holdfast apparatus, is likely a point of highest mechanical stresses and a potential location of skeletal failure, an observation consistent with our simulated buckling locations shown in electronic supplementary material, figure S3.

5. Hydrodynamic analyses

To explore the potential hydrodynamic benefits of the unique maze-like collection of bidirectional helical ridges located on the skeletal tube of *E. aspergillum*, we developed a computational fluid dynamics (CFD) framework, and compared their performance to alternative equal-length ridge geometries that are commonly employed in modern engineering applications for vortex suppression and drag reduction [11–13].

Since the natural habitat of the genus *Euplectella* can vary widely (occurring in low and temperate latitudes at depths ranging from 36 to 5050 m [18]), these sponges are likely to experience a wide range of flow patterns and velocities that must be considered. As such, in our simulations, we considered non-dimensional Reynolds numbers *Re* ranging from 5500 to 60 000, where *Re* was defined as

$$Re = \frac{ul}{\nu}, \tag{5.1}$$

with u being the flow speed, l the characteristic length scale ($2R_o$), and ν the fluid kinematic viscosity. Assuming a representative sponge with diameter $2R_o$ of *ca* 35 mm [4], living in water with temperatures ranging from *ca* 2 to 10°C, this Reynolds number range encompasses a flow velocity u ranging between a biologically relevant *ca* 200 mm s^{-1} and an extremely fast *ca* 2500 mm s^{-1}. It is important to note that the length scale l for all computations does not include the dimensions of the ridges (relating instead to the cylinder outer diameter only), and the resulting *Re* range encompasses a large flow regime, where vortex shedding behind cylindrical structures is known to occur.

5.1. Methods

To model fluid flow around the different cylindrical geometries, we used the CFD package ANSYS CFX, Release 18, which employs a hybrid finite-volume/finite-element approach to discretizing the Navier–Stokes equations governing fluid flow. The systems of equations were solved using an unsteady fully-implicit, fully-coupled multi-grid second-order backward Euler solver in the laboratory frame of reference. The shear stress transport turbulence model [21], which combines the k–ω model near the wall and the k–ϵ model away from the wall, was used throughout this study. This choice of turbulence model ensured accurate prediction of onset and amount of flow separation under adverse pressure gradient conditions. This approach also allowed the model to handle transitions of the flow from laminar to turbulent, accurately refining the flow profile around the complex geometry of the ridges. It is important to note that in our CFD simulations, we did not account for interactions between the flow and the mechanical deformation of the sponge (i.e. we did not perform fluid–structure interaction simulations).

In the hydrodynamic simulations, we focused on comparing one representative sponge ridge design (from the ten mapped), specifically *Sponge 1* shown in figure 3*c*, to the *Unidirectional* and *Bidirectional* configurations for cylindrical cores with both *Small* and *Large Pores*. All models with a porous cylindrical core were placed at the bottom of a rectangular prism-shaped fluid domain, with size $40R_o \times 80R_o \times 20H$, to which symmetry condition on the top face and a slip condition on the bottom face were applied (see electronic supplementary material, figure S4, for details). The resulting configuration thus consisted of a porous hollow cylinder with a closed bottom and an open top, functionally analogous to the geometry of the native sponge. The use of a finite length cylinder in a large domain for the porous hydrodynamic simulations was chosen in order to simulate the flow profile through the sponge interior, thus permitting the quantification of any

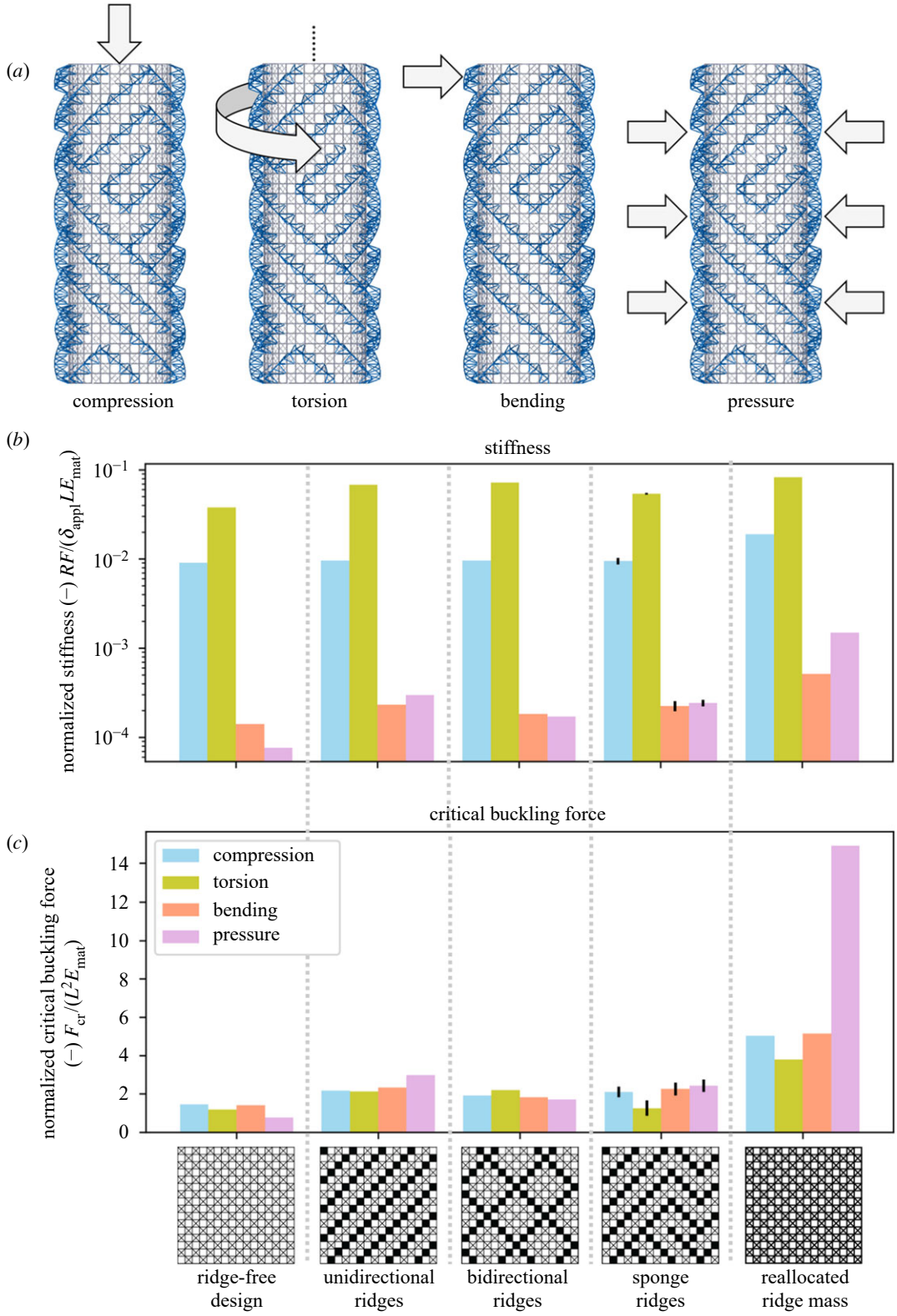

Figure 5. Structural analyses. (*a*) Schematics illustrating boundary conditions considered in the FE simulations. For all considered loading conditions, the displacement at the bottom was held fixed, namely $u_x = u_y = u_z = 0$, and a displacement δ_{appl} (indicated with arrows) was applied. (*b*,*c*) Bar plots showing normalized stiffness $RF/(\delta_{appl}LE_{mat})$ and normalized critical buckling force $F_{cr}/(L^2E_{mat})$ with different colours corresponding to each loading condition. The models considered were the 10 mapped *Sponge* geometries (see electronic supplementary material, figure S1), the *Unidirectional* and *Bidirectional* geometries, the *Ridge-Free* design, and the *Reallocated Ridge Mass* design, from left to right, respectively. For the *Reallocated Ridge Mass* design, we employed the *Ridge-Free* design, but reallocated the volume from the ridges into the cylinder elements, thus making each element thicker and more robust.

changes in induced flow. To facilitate direct comparisons to previously published results [15,22], the models with a non-porous cylindrical core were placed in a fluid domain with size $40R_o \times 80R_o \times H$, to which we applied periodic boundary conditions at the top–bottom faces (see electronic supplementary material, figure S5, for details). For all analyses, we then imposed a uniform flow velocity perpendicular to one of the side walls, zero pressure to the opposite face and slip conditions on the remaining two side walls. Finally, we imposed no-slip conditions on the boundaries of the

cylindrical structure. For each model, we conducted simulations to calculate the following.

— *Lift coefficient:* For each timestep, we obtained the coefficient of lift as

$$C_L = \frac{2F_L}{\rho A u^2}, \tag{5.2}$$

where F_L was obtained by integrating the perpendicular-to-flow component of the pressure acting on all external faces of the cylindrical structure, ρ was the fluid density, A was the surface area of all external faces of the cylindrical structure, and u was the flow velocity.

— *Shedding frequency:* Once C_L was computed as a time series, we performed a power spectral density (PSD) analysis on the C_L data to obtain a power spectrum of frequencies for the lift force. To obtain the PSD for the time series, we computed the Fourier decomposition of the signal and analysed the relative magnitudes of each of the coefficients. In this analysis, the shedding frequency is identified as the highest power frequency, if shedding exists. Note that in order to ensure that the vortex shedding results were reproducible for perturbations within the sponge ridge design space (in addition to *Sponge 1*), we also performed a the PSD analysis on two additional sponge ridge configurations (*Sponges 2* and *3* in electronic supplementary material, figure S3).

— *Drag coefficient:* To measure the drag on the structure, we computed the coefficient of drag for each time-step, which was defined as

$$C_D = \frac{2F_D}{\rho A u^2}, \tag{5.3}$$

where F_D was obtained by integrating the parallel-to-flow component of the pressure acting on all external faces of the cylindrical structure. Note that in order to validate our simulations, we compared our results for a cylinder without pores and without ridges to the drag coefficient data obtained from Blevins [15] (see electronic supplementary material, figure S6(b), for more information).

— *Flow profile through the openings in the cylindrical core:* To investigate the potential role of the ridges as a mechanism for increasing/redirecting fluid flow through the sponge for feeding/gas exchange purposes, we created a closed cylindrical boundary matching the geometry of the sponge's interior and computed the time-averaged flow profile through the openings in the sponge's body wall by averaging the flow over three cycles of shedding. Using this flow profile, we integrated the absolute value of the flow rate over the area A of the cylindrical boundary and top of the sponge defined by

$$V = \int_A \frac{1}{2}\left|\frac{\dot{V}}{A}\right| \mathrm{d}A. \tag{5.4}$$

Note, that because of fluid incompressibility and conservation of mass, the volume flow in the boundary V_{in} must equal the volume out V_{out} leading to a division by 2 to obtain total volume exchanged.

To balance model accuracy and computational efficiency, in all our simulations we refined the mesh near the region of interest (in the sponge's vicinity) and kept the far-field meshing coarse. For each of the models, we produced a mesh consisting of more than 2 million elements, an illustration of which can be found in electronic supplementary material, figure S7.

5.2. Results

In figures 6, 8 and 10, we report the lift coefficient, shedding frequency and drag coefficient (together with numerical snapshots that show the vorticity fields) at $Re = 5500$ for designs comprising a hollow cylindrical core with *No Pores*, *Small Pores* ($\phi_s \approx 0.06$) and *Large Pores* ($\phi_s \approx 0.41$), respectively. For all three cases, we considered three different ridge geometries (*Unidirectional*, *Bidirectional* and *Sponge* configurations) and compared their performance to a ridge-free control.

As shown in figure 6*a*,*b* we find that for the geometries with non-porous cylindrical cores and either *Bidirectional* ridges or no ridges, there exists large cyclic lift forcing acting on the structures. By contrast, we see that for the *Sponge* and *Unidirectional* ridge designs, the cyclic forcing is quickly suppressed. The PSD analysis performed on these lift data reveals that the *Sponge* and *Unidirectional* ridge designs are effective at suppressing vortex shedding forcing on the cylindrical structure, as evident by the lack of a localized peak in figure 6*c*. By contrast, we observe vortex shedding behind the cylinder for both the ridge-free and *Bidirectional* ridge configurations, with the vortices actually amplified by the bidirectional ridge design (as indicated by a higher PSD peak in figure 6*c*). It is also important to note that while the *Unidirectional* ridge design shifts the shedding downstream, the *Sponge* ridge design completely suppresses the vortex shedding behind its cylindrical structure (see snapshots in figure 6*e*), demonstrating a more efficient vortex suppression mechanism. While the *Sponge* ridge design outperforms the *Unidirectional* ridge design in vortex suppression, it does, however, lead to a slightly increased drag force on the structure (figure 6*d*).

To validate our results, we first compared both the location of the PSD peak and the drag coefficient obtained for a non-porous cylindrical core without ridges to existing empirical data for a cylinder in a uniform two-dimensional flow at $Re = 5500$ (black dashed lines in figure 6*c*,*d*—for more information, see electronic supplementary material, figure S6) [15,22]. The good agreement between these two datasets confirmed the suitability of our numerical approach. To further validate the effects of vortex shedding observed for our selected sponge ridge geometry with a non-porous cylindrical core, in figure 7, we analysed the PSD for two additional *Sponge* ridge designs (*Sponge 2* and *Sponge 3* from electronic supplementary material, figure S1), in addition to the original sponge design (*Sponge 1*), the *Unidirectional*, the *Bidirectional*, and the ridge-free geometries. In this plot, we observe that all three of the sponge-inspired designs efficiently suppress vortex shedding compared to the other more symmetrical ridge geometries. These results thus demonstrate that the observations presented in figure 6 are likely not specific to the unique sponge ridge geometry investigated.

In figure 8, we report results for designs comprising a hollow cylinder with small pores. For this case, we find that large cyclic lift forcing acting on the structure exists only for the model without ridges (figure 8*a*). We also note that for the *Bidirectional* and *Sponge* ridge geometries, the lift coefficient does not average to zero, since the ridges

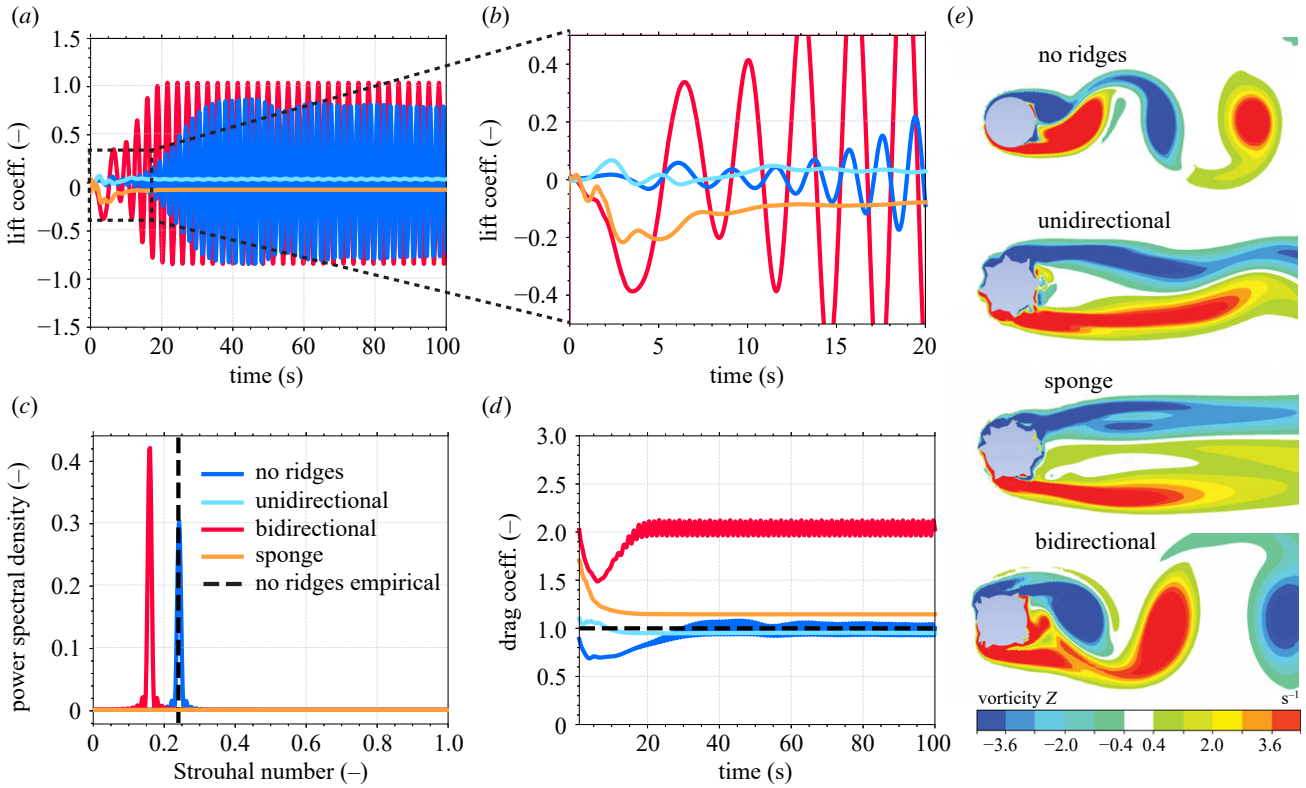

Figure 6. Hydrodynamic results for the different non-porous model geometries, at $Re = 5500$. (*a*) Plot showing transient lift coefficient C_l for the different geometries. (*b*) Magnified view of transient lift coefficients, showing the initial shedding behaviour for the different model geometries. (*c*) Plot showing power spectral density (PSD) as a function of Strouhal number for the different model geometries. The vertical dashed black line shows the empirical Strouhal number for a smooth cylinder using a $Re = 5500$ flow regime. Note that the last 20 s of the transient data (when the flow reaches a periodic state) were used to compute the PSD. (*d*) Plot showing transient drag coefficient C_d for the different model geometries. The horizontal black dashed line corresponds to empirical drag coefficient data for a smooth cylinder. (*e*) Vorticity fields illustrating shedding for the different model geometries.

break the flow symmetry and bias the lift coefficient to a particular direction (see electronic supplementary material, figure S8, for more information). By taking the data from the lift coefficient and computing the PSD, we observe that for this level of biologically relevant porosity, prominent vortex shedding still exists behind the ridge-free geometry (figure 8*c*), while all three models with ridges are capable of suppressing vortex shedding. As such, these results demonstrate that for $\phi_s \approx 0.06$, the introduction of helical ridges is sufficient to suppress vortex shedding regardless of the specific ridge arrangement. However, although all three ridge geometries suppress the vortices over the long term, it is important to note that some geometries provide a faster dissipation mechanism than others. As shown in figure 8*b*, the *Unidirectional* and *Bidirectional* ridge designs exhibit cyclical lift forcing as soon as flow is initiated, indicating an early onset of vortex shedding, and whose amplitude is partially dissipated over time. The *Sponge* ridge design, in contrast, transitions much earlier to a steady flow profile with no indication of cyclical lift forcing. Such rapid suppression of vortex shedding is of biological relevance to the sponge, since its local environment can be prone to fluctuations in flow velocity depending on the depth at which it occurs. Finally, the results shown in figure 8*d* demonstrate that the choice of ridge design has also implications on the drag imposed on the cylindrical structure, with the *Bidirectional* design increasing the drag substantially compared to the other ridges geometries.

While the hydrodynamic results reported thus far are for $Re = 5500$ (a value relevant to the natural habitat of the

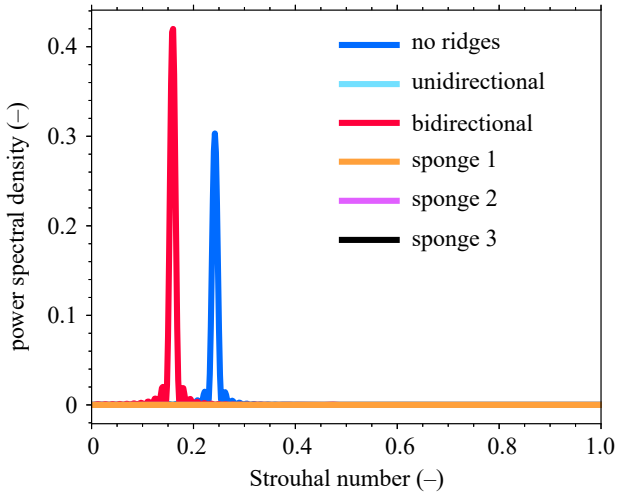

Figure 7. PSD analysis of additional *Sponge* ridge geometries. PSD plot comparing the different considered structures (from figure 6) to ridge designs obtained from two additional *Sponge* samples (see electronic supplementary material, figure S1). It should be noted that all three of the *Sponge* data lines are indistinguishable and superimposed. Results presented for $Re = 5500$.

sponge), in figure 9, we also investigated the effect of other Reynolds numbers on these observed behaviours. Specifically, we considered $Re = 15\,000$ and $Re = 60\,000$ and, due to the computational complexity of these simulations, compared the hydrodynamic performance of a cylindrical tube with *Small Pores* and *Sponge* ridge design to that of a cylindrical tube with *Small Pores* and *No Ridges*. We find that for both

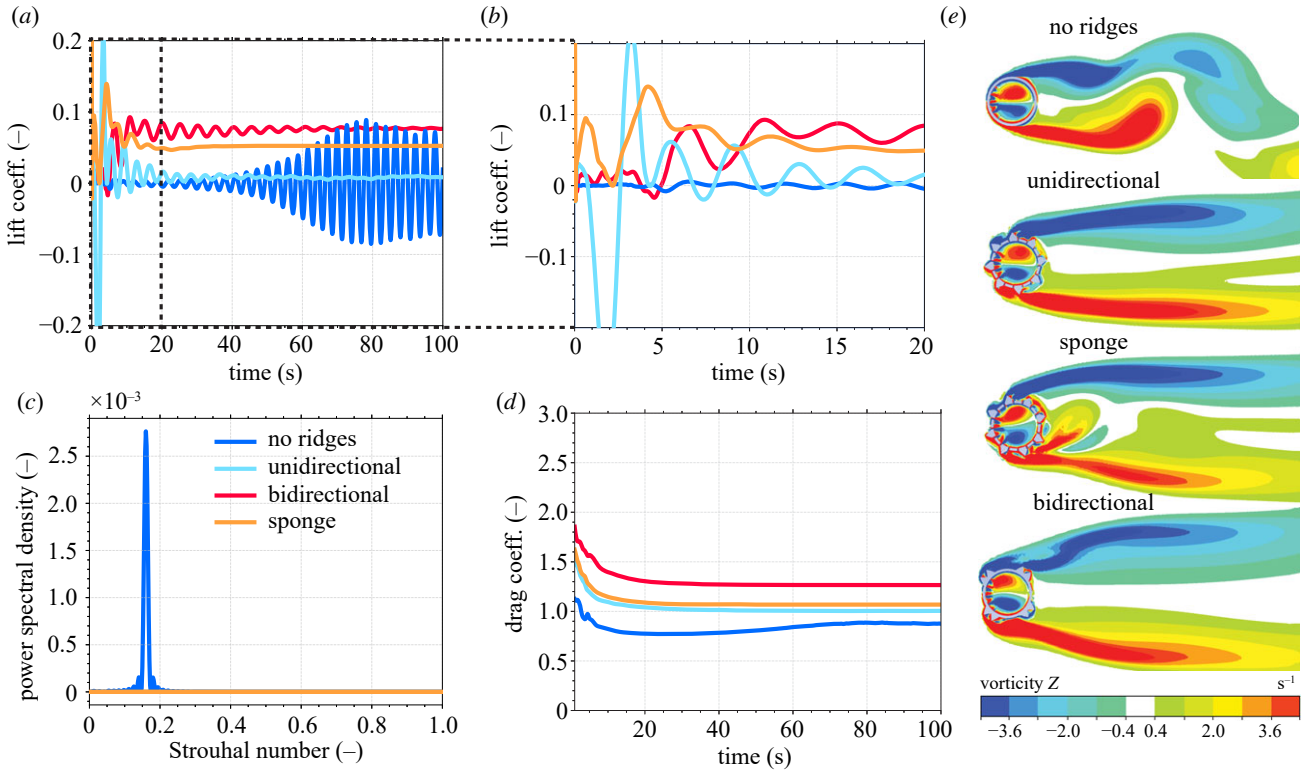

Figure 8. Hydrodynamic results for the different model geometries exhibiting biologically relevant (small) porosities, approximating the anatomy of living sponges, at $Re = 5500$. (*a*) Plot showing transient lift coefficient C_l for the different model geometries. (*b*) Magnified view of transient lift coefficients, showing the initial shedding behaviour for the different model geometries. (*c*) Plot showing power spectral density (PSD) as a function of Strouhal number for the different model geometries. Note that the last 20 s of the transient data (when the flow reaches a periodic state) were used to compute the PSD. (*d*) Plot showing transient drag coefficient C_d for the different model geometries. (*e*) Vorticity fields illustrating shedding for the different model geometries.

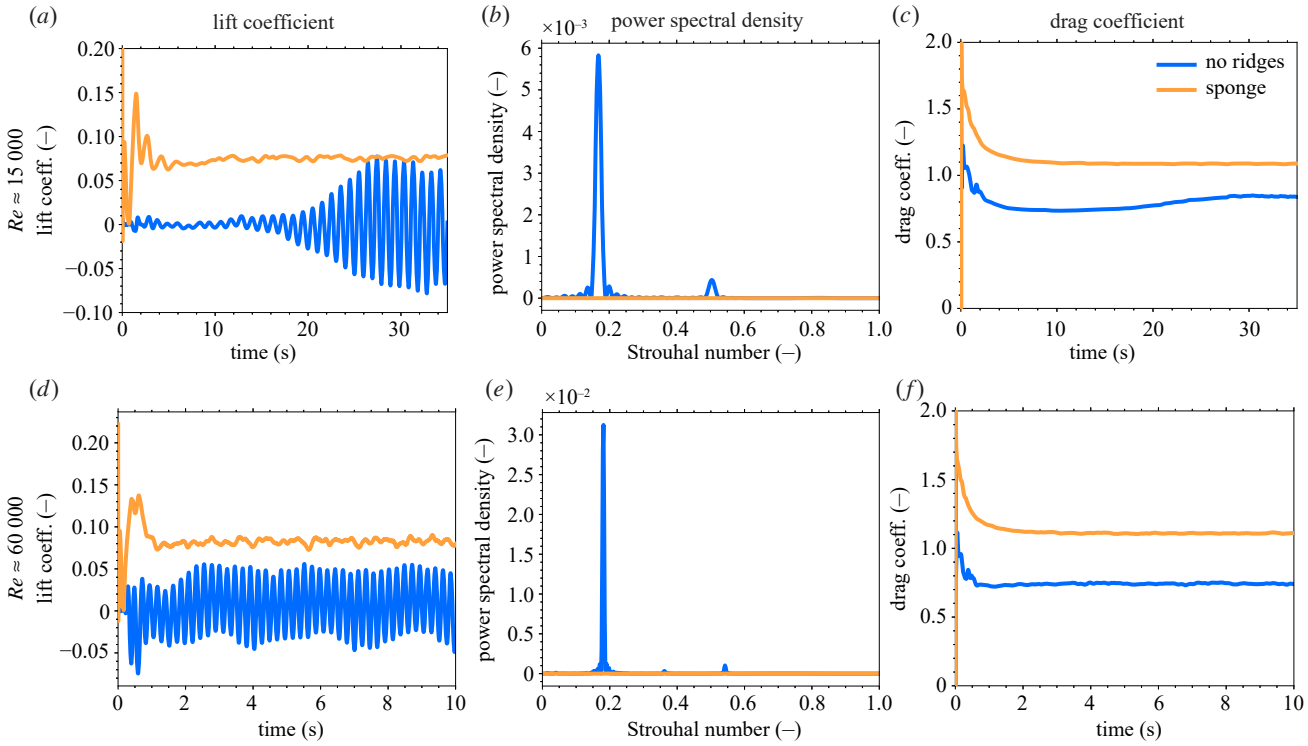

Figure 9. Hydrodynamics results for the low-porosity ridge-free and *Sponge* geometries, at $Re = 15\,000$ and $Re = 60\,000$. (*a*) Plot showing transient lift coefficient C_l as a function of time at $Re = 15\,000$. (*b*) PSD plot, with frequency converted to Strouhal number. Note that the last 10 s of the transient data were used to compute the PSD at $Re = 15\,000$. (*c*) Plot showing transient drag coefficient C_d as a function of time at $Re = 15\,000$. (*d*) Plot showing transient lift coefficient C_l as a function of time at $Re = 60\,000$. (*e*) PSD plot, with frequency converted to Strouhal number at $Re = 60\,000$. Note that the last 5 s of the transient data were used to compute the PSD. (*f*) Plot showing transient drag coefficient C_d as a function of time at $Re = 60\,000$.

considered Reynolds numbers, the trends observed in figure 8 are unchanged for lift coefficients, shedding frequencies, and drag coefficients.

Finally, in figure 10, we report the hydrodynamic results for models with a large surface porosity ($\phi_s \approx 0.42$), approaching that of a cleaned (bare) sponge skeleton. The results show

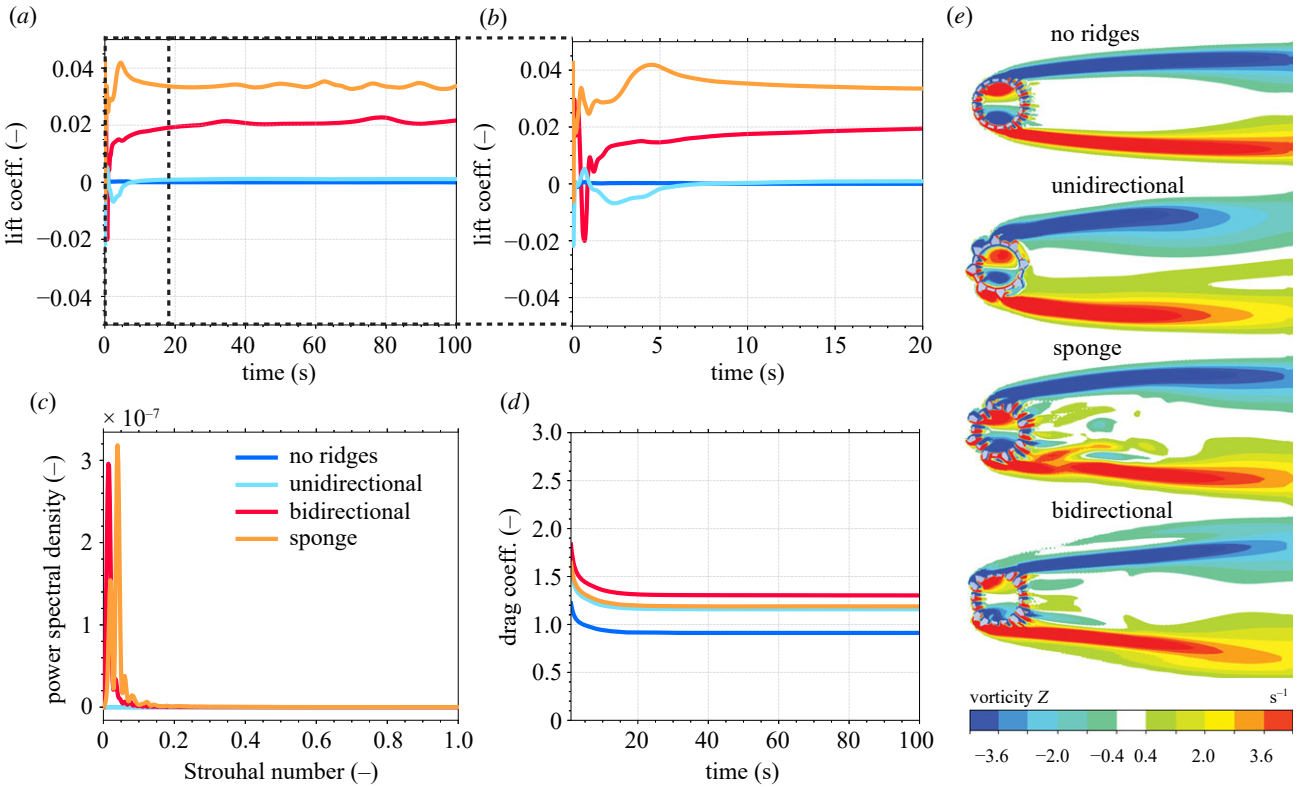

Figure 10. Hydrodynamic results for the different model geometries exhibiting (large) porosities, approximating only the skeletal anatomy of tissue-free sponges, at $Re = 5500$. (*a*) Plot showing transient lift coefficient C_l for the different model geometries. (*b*) Magnified view of transient lift coefficients, showing the initial shedding behaviour for the different model geometries. (*c*) Plot showing power spectral density (PSD) as a function of Strouhal number for the different model geometries. Note that the last 20 s of the transient data (when the flow reaches a periodic state) were used to compute the PSD. (*d*) Plot showing transient drag coefficient C_d for the different model geometries. (*e*) Vorticity fields illustrating shedding for the different model geometries.

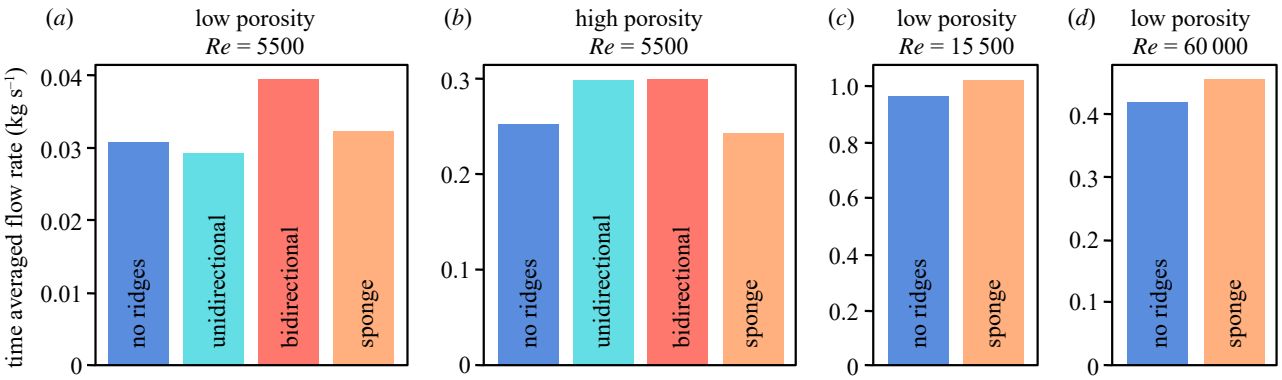

Figure 11. Quantification of flow rate through the different investigated model geometries. Bar plots showing time-averaged flow rate through the walls of the (*a*) low-porosity and (*b*) high-porosity models, at $Re = 5500$, and the low-porosity models at (*c*) $Re = 15\,000$ and (*d*) $Re = 60\,000$.

two key trends. First, we find that at this level of porosity, the existence of von Kármán vortices is not prominent for any of the models, as indicated by the lack of cyclic lift forcing acting on the structures shown in figure 10*a*,*b*. These results therefore suggest that the introduction of ridges is unnecessary for this level of porosity and that there exists a transition in the flow for surface porosities somewhere between $\phi_s \approx 0.06$ and $\phi_s \approx 0.42$. Second, the results shown in figure 10*c* also demonstrate that for large surface porosities, the drag coefficient remains dependent on the ridge arrangements, and that the dependency is similar to that observed in figure 8*d* for $\phi_s \approx 0.06$.

Beyond the vortex suppression and drag reduction properties of the sponge's external ridges, we also investigated their potential role as a mechanism for increasing/redirecting fluid flow through the sponge for feeding/gas exchange purposes. Towards this end, in figure 11*a*,*b*, we report the time averaged flow rate over the area of the cylindrical core (defined as in (5.4)) at $Re = 5500$ for all considered different geometries with a cylindrical core with both *Small* and *Large Pores*, respectively. These results demonstrate that the flow through the walls of the cylinder (and out the terminal opening) for the *Sponge* design is almost identical to that of the model without ridges, whereas the *Unidirectional* or *Bidirectional* ridges lead to a slight increase in flow. Similar trends were also observed for $Re = 15\,000$ (figure 11*c*) and $Re = 60\,000$ figure 11*d* in the case of *Small Pores* geometry, suggesting that the presence of the *Sponge* ridge design does not offer significant

added mass flow through the walls of the main cylinder across a wide range of flow regimes. It should be noted that the path of water flow through the body wall of living specimens of *Euplectella aspergillum* follows a more convoluted trajectory than the simple linear channel modelled in the present study, thus potentially reducing the overall flow rate of water through the sponge in comparison to our predicted values. While this may be the case, these induced flow effects, which have been well documented in previous studies [23,24] are largely driven by flow-induced pressure differentials across the sponge's tubular form, and as such, the general trends reported here are likely to be unaffected by slight variations in through-wall flow rates.

6. Conclusion

To summarize, using a combination of FE simulations and computational fluid mechanics, in this study we explored the potential multi-functionality of the complex network of external maze-like ridges found in the skeletal system of the marine sponge, *Euplectella aspergillum*. Using this integrated approach, we demonstrate that this complex ridge system offers the sponge an efficient mechanism for rapidly suppressing von Kármán vortex shedding and reducing lift forcing oscillations (which may be essential for keeping the sponge anchored into the soft sediments of the sea floor), while at the same time, improving its skeleton's mechanical performance. Beyond their ability to suppress vortex-induced vibrations, which could weaken the attachment point between the sponge's holdfast apparatus and its surrounding substrate, the ridges also likely play a critical role in preventing substrate-associated turbulence and subsequent sediment excavation (see electronic supplementary material, video 1), as has been demonstrated for other bottom-anchored cylindrical geometries under flow [25,26]. The prevention of sediment transport from the down-stream side of the sponge is likely of critical importance to the sponge's survival, since excavation near its holdfast apparatus would also compromise its ability to remain anchored into the soft sediments of the sea floor.

To explore the additional benefits of its maze-like organization, we also compared the sponge ridge geometry to helical strake-based vortex shedding suppression systems commonly employed for above ground (e.g. antennas, and smokestacks) and underwater (support beams, vertical pipelines) high aspect ratio cylindrical structures. From these studies, we find that the sponge's ridge design can completely suppress vortex shedding, a behaviour which differs from that of more symmetrical helical strake configurations, which either delay shedding downstream (*Unidirectional* ridge design) or amplify the shedding magnitude (*Bidirectional* ridge design). Further, we demonstrate that the *Sponge* ridge design continues to effectively suppress vortex shedding across a wide range of flow regimes.

While the findings of this study provide new insight into the multi-functionality (mechanical and hydrodynamic) of the complex external ridges in the skeleton of *E. aspergillum*, it is important to note that the flow regimes considered in this study (*Re* between 5500 and 60 000) are also relevant for many man-made cylindrical structures including smokestacks, antennas, submerged piping and offshore floating platforms. As such, the geometric features identified by this study could be directly used in engineering applications where effective dissipation of vortex shedding is necessary, and where vortex-induced vibrations are to be avoided.

Data accessibility. Data and supporting materials are available at https://git.fer.me/sponge-ridges.

Authors' contributions. M.F., K.B. and J.W. conceived the study and developed the methods. M.F., P.C., C.I., T.S. and J.W. created all CAD models for this study. G.M. and J.W. calculated the volume fractions of the different skeletal features. M.F. and P.C. carried out the finite-element modelling. M.F. and M.S. carried out the hydrodynamic modelling. M.F., M.S., H.H., K.B. and J.W. contributed to the analysis of results. M.F., M.S., K.B. and J.W. contributed to the writing of the manuscript. M.F., H.H., K.B. and J.W. secured funding for this project. All authors provided valuable feedback and approved the final manuscript.

Competing interests. We declare we have no competing interests.

Funding. This work was supported by NSF-GRFP Fellowship (grant no. DGE-1144152) (M.C.F.), a GEM Consortium Fellowship (M.C.F.) and the Harvard Graduate Prize Fellowship (M.C.F.), and was partially supported by the NSF through the Harvard University Materials Research Science and Engineering Center (grant no. DMR-2011754) and NSF DMREF (grant no. DMR-1922321).

Acknowledgements. We thank George Lauder, Mark Scott, Jochen Mueller, Joanna Aizenberg, Chris Rycroft and Joost Vlassak for insightful discussions.

References

1. Aizenberg J, Weaver JC, Thanawala MS, Sundar VC, Morse DE, Fratzl P. 2005 Skeleton of *Euplectella* sp.: structural hierarchy from the nanoscale to the macroscale. *Science* **309**, 275–278. (doi:10.1126/science.1112255)
2. Monn MA, Weaver JC, Zhang T, Aizenberg J, Kesari H. 2015 New functional insights into the internal architecture of the laminated anchor spicules of *Euplectella aspergillum*. *Proc. Natl Acad. Sci. USA* **112**, 4976–4981. (doi:10.1073/pnas.1415502112)
3. Monn MA, Ferreira J, Yang J, Kesari H. 2017 A millimeter scale flexural testing system for measuring the mechanical properties of marine sponge spicules. *JoVE (Journal of Visualized Experiments)* **112**, e56571–e56571.
4. Weaver JC *et al.* 2007 Hierarchical assembly of the siliceous skeletal lattice of the hexactinellid sponge *Euplectella aspergillum*. *J. Struct. Biol.* **158**, 93–106. (doi:10.1016/j.jsb.2006.10.027)
5. Weaver JC *et al.* 2010 Unifying design strategies in demosponge and hexactinellid skeletal systems. *J. Adhesion* **86**, 72–95. (doi:10.1080/00218460903417917)
6. Monn MA, Vijaykumar K, Kochiyama S, Kesari H. 2020 Lamellar architectures in stiff biomaterials may not always be templates for enhancing toughness in composites. *Nat. Commun.* **11**, 373. (doi:10.1038/s41467-019-14128-8)
7. Fernandes MC, Aizenberg J, Weaver JC, Bertoldi K. 2020 Mechanically robust lattices inspired by deep-sea glass sponges. *Nat. Mater.* **20**, 237–241. (doi:10.1038/s41563-020-0798-1)
8. Havens BT, Klaiber FW, Lohnes RA, Zachary LW. 1995 Longitudinal strength and stiffness of corrugated steel pipe. *Transp. Res. Rec.* **1514**, 1–9.
9. Kang JS, Stuart SJ, Davidson JS. 2013 Analytical evaluation of maximum cover limits for thermoplastic pipes used in highway construction. *Struct. Infrastruct. Eng.* **9**, 667–674. (doi:10.1080/15732479.2011.604090)

10. Yazdani M, Rahimi GH. 2010 The effects of helical ribs' number and grid types on the buckling of thin-walled gfrp-stiffened shells under axial loading. *J. Reinf. Plast. Compos.* **29**, 2568–2575. (doi:10.1177/0731684409355202)
11. Gao Y, Yang J, Xiong Y, Wang M, Peng G. 2016 Experimental investigation of the effects of the coverage of helical strakes on the vortex-induced vibration response of a flexible riser. *Appl. Ocean Res.* **59**, 53–64. (doi:10.1016/j.apor.2016.03.016)
12. Quen LK, Abu A, Kato N, Muhamad P, Tan LK, Kang HS. 2018 Performance of two-and three-start helical strakes in suppressing the vortex-induced vibration of a low mass ratio flexible cylinder. *Ocean Eng.* **166**, 253–261. (doi:10.1016/j.oceaneng.2018.08.008)
13. Ranjith ER, Sunil AS, Pauly L. 2016 Analysis of flow over a circular cylinder fitted with helical strakes. *Procedia Technol.* **24**, 452–460. (doi:10.1016/j.protcy.2016.05.062)
14. Williamson CHK. 1996 Vortex dynamics in the cylinder wake. *Annu. Rev. Fluid Mech.* **28**, 477–539. (doi:10.1146/annurev.fl.28.010196.002401)
15. Blevins RD. 1986 *Flow-induced vibration*. Malabar, FL: Rebert E. Kridger Publishing Co.
16. Kármán Tv. 1912 Über den mechanismus des wiederstandes, den ein bewegter körper in einer flüssigkeit erfährt. *Nachrichten von der Gesellschaft der Wissenschaften zu Göttingen, Mathematisch-Physikalische Klasse* **1912**, 547–556.
17. Kármán Tv. 1911 Über den mechanismus des widerstandes, den ein bewegter körper in einer flüssigkeit erfährt. *Nachrichten von der Gesellschaft der Wissenschaften zu Göttingen, Mathematisch-Physikalische Klasse* **1911**, 509–517.
18. Hooper J, Van Soest R. 2002 *Systema porifera. A guide to the classification of sponges*. Berlin, Germany: Springer.
19. Schulze FE. 1887 Report on the hexactinellida collected by 'HMS challenger' during the years 1873–1876. *HMS Challenger Sci Results Zool*, 21.
20. Schulze FE. 1904 Hexactinellida. In *Scientific results of the German deep-sea expedition with the steamboat, Valdivia 1898–1899* (ed. C Chun). Jena, Germany: Verlag Gustav Fischer.
21. ANSYS©. 2020 Academic research, release 14.0 help systems. *ANSYS CFX-Solver theory guide*.
22. Anderson JD Jr. 2010 *Fundamentals of aerodynamics*. New York, NY: McGraw-Hill Education.
23. Leys SP, Yahel G, Reidenbach MA, Tunnicliffe V, Shavit U, Reiswig HM. 2011 The sponge pump: the role of current induced flow in the design of the sponge body plan. *PLoS ONE* **6**, e27787. (doi:10.1371/journal.pone.0027787)
24. Vogel S. 1977 Current-induced flow through living sponges in nature. *Proc. Natl Acad. Sci. USA* **74**, 2069–2071. (doi:10.1073/pnas.74.5.2069)
25. Davies AG, Thorne PD. 2005 Modeling and measurement of sediment transport by waves in the vortex ripple regime. *J. Geophys. Res.: Oceans* **110**, C05017. (doi:10.1029/2004JC002468)
26. Stastna M, Lamb KG. 2002 Vortex shedding and sediment resuspension associated with the interaction of an internal solitary wave and the bottom boundary layer. *Geophys. Res. Lett.* **29**, 7-1–7-3. (doi:10.1029/2001GL014070)

Supplementary Information: Mechanical and Hydrodynamic Analyses of Helical Strake-like Ridges in a Glass Sponge

MATHEUS C. FERNANDES[1,2], MEHDI SAADAT[3], PATRICK CAUCHY-DUBOIS[1], CHIKARA INAMURA[4], TED SIROTA[1,2], GARRETT MILLIRON[5], HOSSEIN HAJ-HARIRI[6], KATIA BERTOLDI[1,2], AND JAMES C. WEAVER[1,2,†]

[1] *John A. Paulson School of Engineering and Applied Sciences – Harvard University, Cambridge, MA 02138*
[2] *Wyss Institute – Harvard University, Cambridge, MA 02138*
[3] *Department of Organismic and Evolutionary Biology – Harvard University, Cambridge, MA 02138*
[4] *Media Lab – Massachusetts Institute of Technology, Cambridge, MA 02139*
[5] *Collective Design, Grand Rapids, MI 49505*
[6] *College of Engineering and Computing – University of South Carolina, Columbia, SC 29208*
Corresponding author: †*jweaver@seas.harvard.edu*

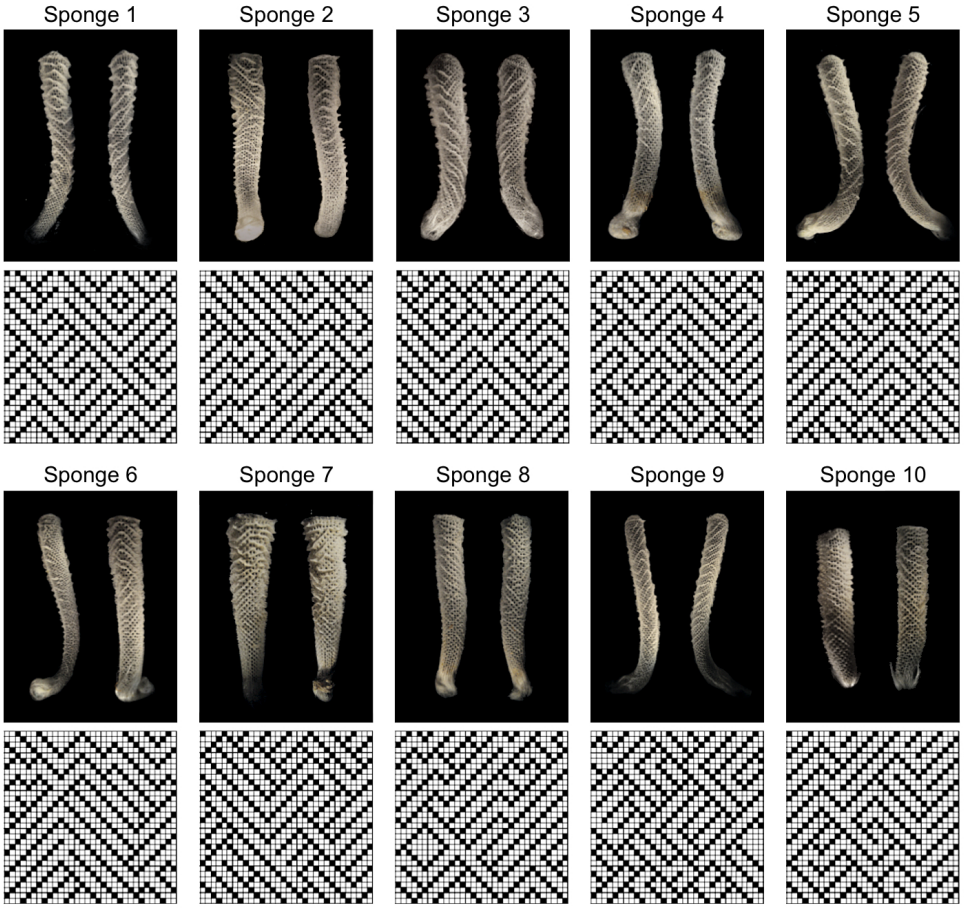

Figure S1: Sponge specimens and their corresponding ridge maps. Photographs of the ten sponge specimens used in this study, each taken from two different orientations (Upper) and their corresponding planar ridge connectivity diagrams (Lower). For each ridge map, filled squares denote the presence, and white squares denote the absence of ridge elements. The photos were all acquired at approximately the same magnifications and their heights average ca. 25 cm, with mid-shaft widths ranging from ca. 3-4 cm. The dry sponge specimens were acquired from commercial sources, and cleaned with a 5 % solution of sodium hypochlorite to remove any residual organic material before imaging.

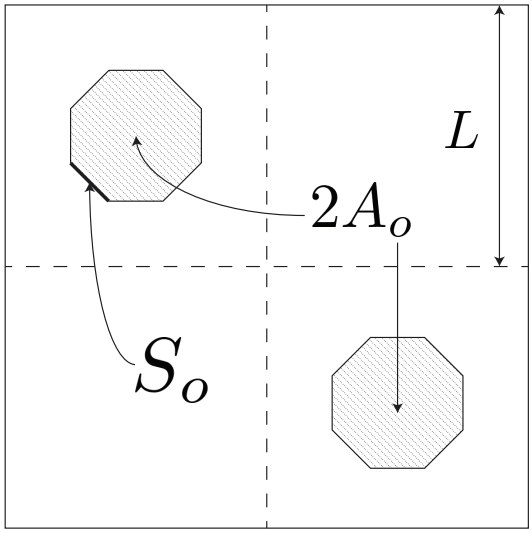

Figure S2: Hydrodynamic analysis: Defining pore size of the hollow cylindrical cores. To calculate the edge length of the octagonal openings introduced into the hollow cylindrical cores, we first defined the effective surface porosity, which is given by

$$\phi_s = \frac{\text{Area of Void}}{\text{Total Area}} = \frac{2A_o}{A_t} = \frac{4(1+\sqrt{2})S_o^2}{4L^2} = (1+\sqrt{2})\left(\frac{S_o}{L}\right)^2,$$

where A_o is the area of each equilateral octagonal opening, A_t is the total area, and S_o is the length of a side from the equilateral octagon. To match the pore size of a living sponge we choose $S_o/L = 0.15703$, so that

$$\phi_s = (1+\sqrt{2})\,(0.15703)^2 = 0.05953.$$

In this configuration, the geometry exhibits a 5.953% void fraction and a $(100\% - 5.953\%) = 94.047\%$ solid fraction (we refer to this model as the *cylindrical core with small pores*).

When choosing $S_0/L = \sqrt{2} - 1$ to reflect the porosity of only the skeletal components (corresponding to a cleaned/bare sponge skeleton), the effective surface porosity is given by

$$\phi_s = \frac{\text{Area of Void}}{\text{Total Area}} = \frac{2A_o}{A_t} = \frac{4\sqrt{2}-4}{4} = 0.4142.$$

In this configuration, the geometry exhibits a 41.42% void fraction and a $(100\% - 41.42\%) = 58.58\%$ solid fraction (we refer to this model as to the *cylindrical core with large pores*).

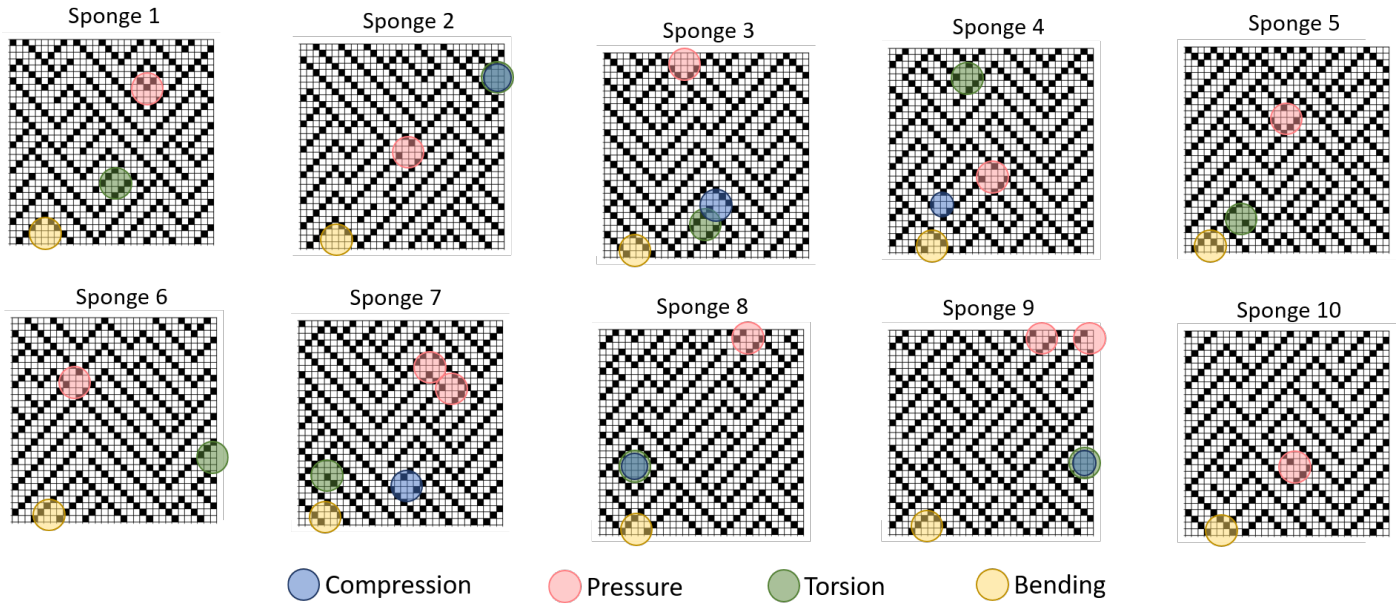

Figure S3: Structural analysis: Buckling locations. FE model predictions of the locations of failures for each of the considered designs and loading conditions. Circles denote the locations where the deformation is expected to localize. For the *Bending* cases, we report results only for one direction of loading, and consistently, the placement of the yellow circles corresponds to the location (at the base of the sponge) immediately opposite of the side of the applied load. A missing circle for a particular structure or loading conditions is indicative of a global deformation under that specific loading regime.

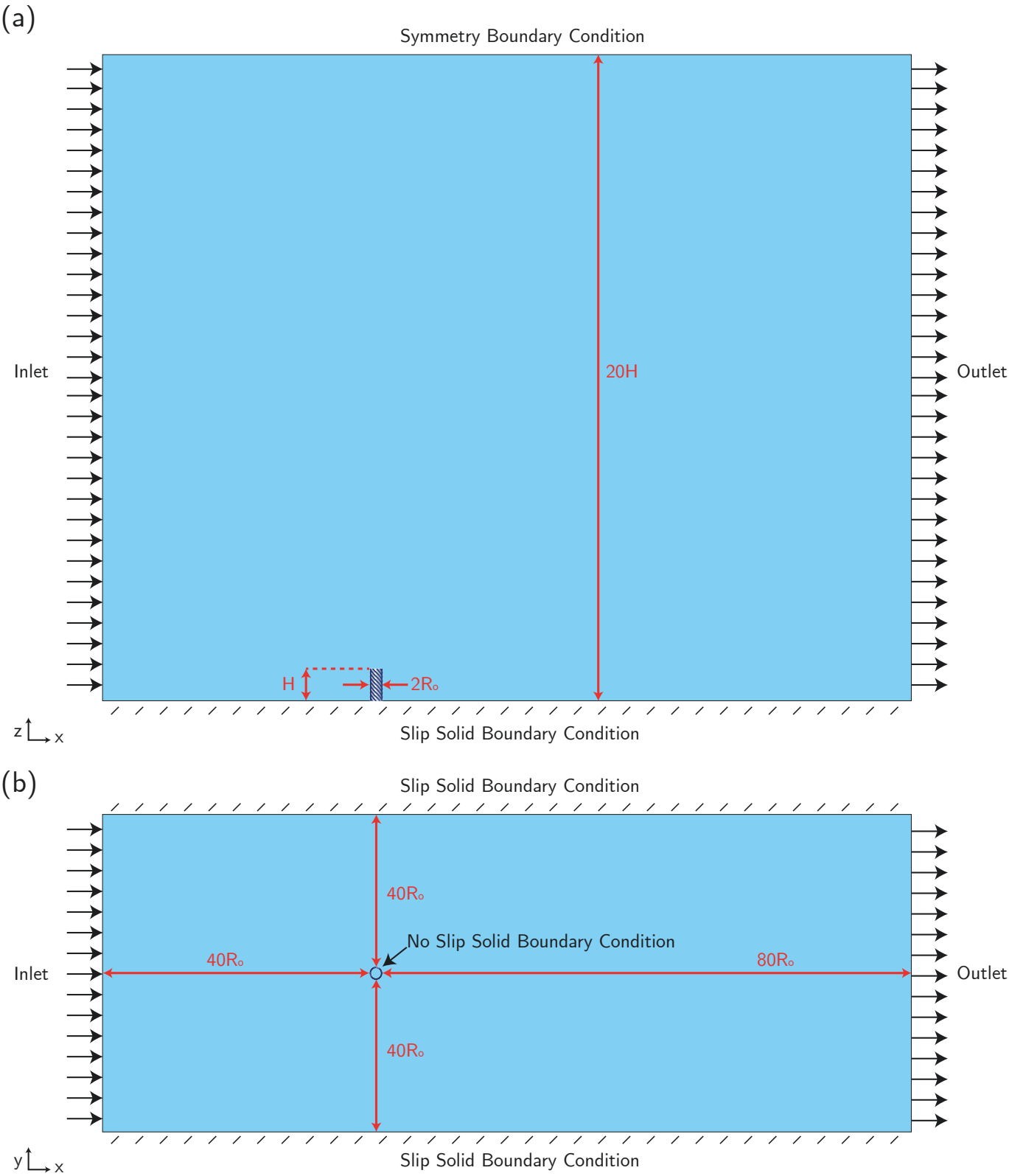

Figure S4: Hydrodynamic analysis: Fluid domain used for models with porous cylindrical cores. The fluid domain (shown schematically from both (a) side and (b) top views) is a rectangular cuboid with size $40R_o \times 80R_o \times 20H$, where $R_o = 23.5$ mm and $H = 146$ mm. The cuboid was positioned to align with the bottom of the cylindrical geometries, leaving a large gap between the top of the cylindrical geometry and top face of the domain to account for flow above and through the cylindrical structures (the schematics also show the applied boundary conditions and is drawn to scale). For these geometries, the dimensions exceed literature suggestions to minimize computational edge effects on the flow profile near the cylindrical geometry [1].

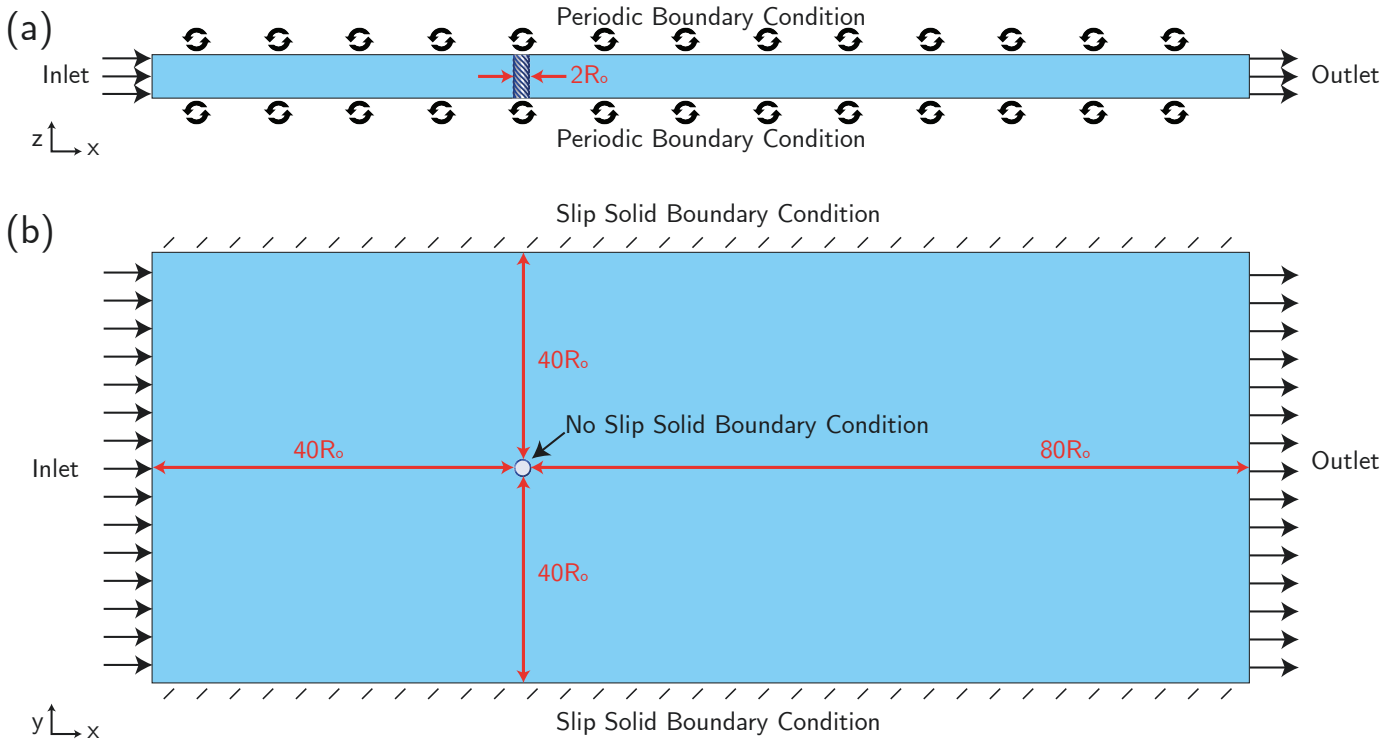

Figure S5: Hydrodynamic analysis: Fluid domain used for models with non-porous cylindrical cores. The fluid domain (shown schematically from both (a) side and (b) top views) is an elongated rectangular cuboid with size $40R_o \times 80R_o \times H$ fully encapsulating the cylindrical geometry. The cuboid domain was constructed around the geometry such that its top and bottom faces match the height H of the cylindrical geometry. The remaining four faces of the cuboid domain were aligned away from the central axis of the cylinder at a distance $40R_o$ from the inlet face, $80R_o$ from the outlet face and $40R_o$ from the other two faces (the schematics also show the applied boundary conditions and is drawn to scale). For these geometries, the dimensions exceed literature suggestions to minimize computational edge effects on the flow profile near the cylindrical geometry [1].

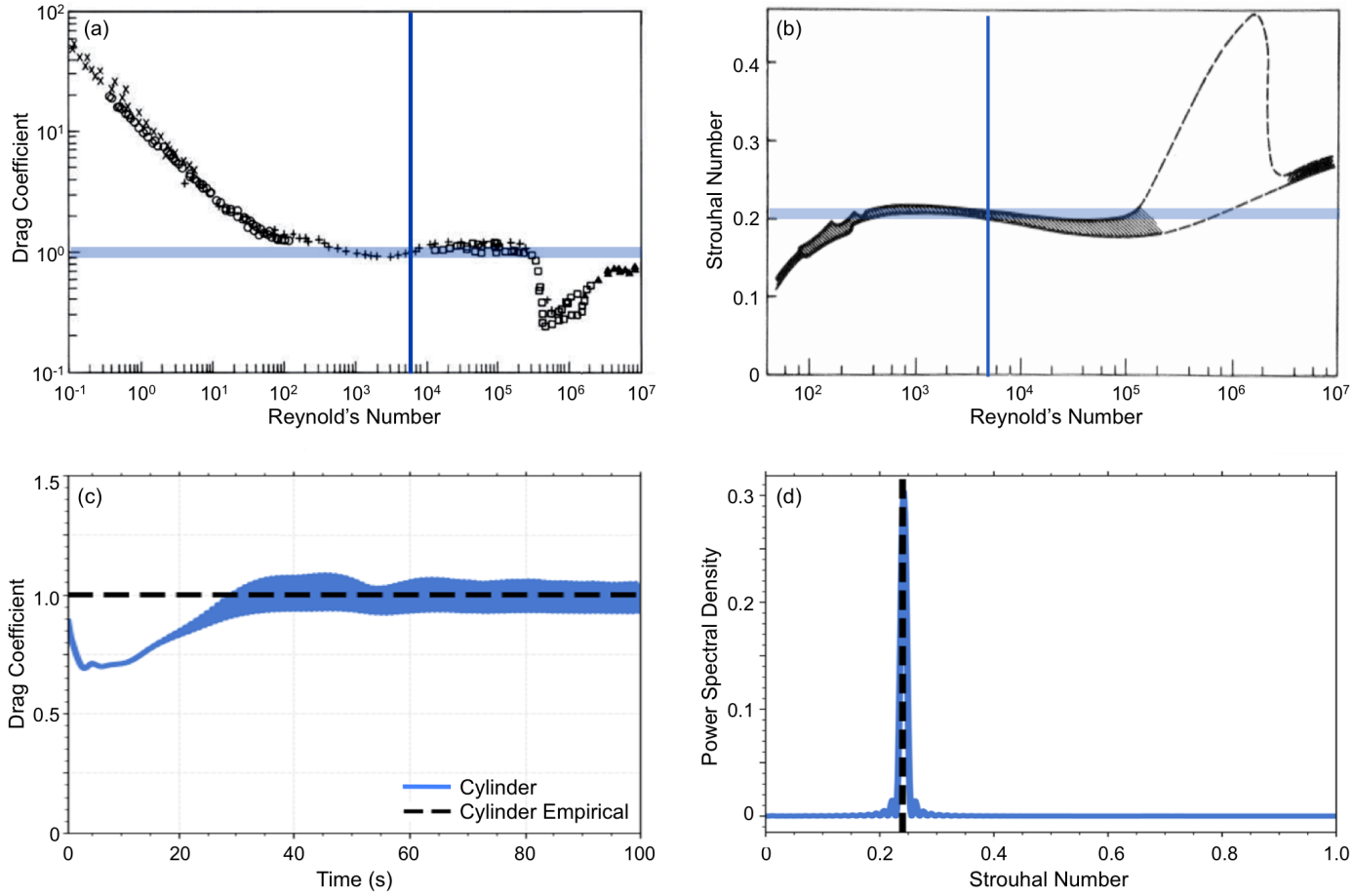

Figure S6: Hydrodynamic analysis: Validation. To validate our hydrodynamic simulations, we considered a flow past the most simple model, specifically, a solid cylinder without ridges. We obtained both the Strouhal number and drag coefficient from our analyses and compared them to established empirical data for a flow passed a bluff cylinder[2,3]. (a) shows literature data for drag coefficient as a function of Reynolds number[3] and (b) shows literature data reported for Strouhal number as a function of Reynolds number[2]. By comparing these data with our results, we find that they closely match with a margin of error under 2% (see (c) and (d)). For the drag coefficient measurements shown in (c), it is important to note that to obtain comparable measurements, we averaged over the shedding oscillation. For both (c) and (d) the simulation results are shown in blue and the empirical data in black dashed lines.

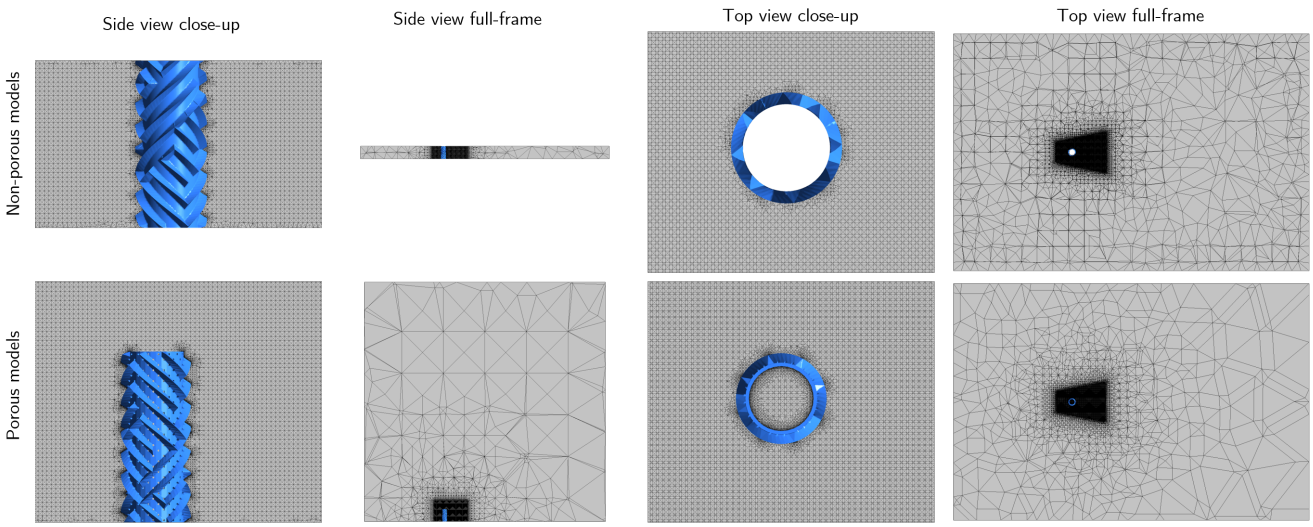

Figure S7: Hydrodynamic analysis: Meshing details. Numerical snapshots exported from *Ansys*® showing the meshes employed in our hydrodynamic analyses. The top row shows the mesh employed for the non-porous models and bottom row shows the mesh for the porous models. All meshes were generated using *Ansys*® *Academic Research ICEM-CFD, Release 2019 R3* and were refined at the region of interest, near and behind the cylinder in order to accurately capture the shear layer separation as well as the vortex shedding formation. The maximum node separation at the surface of the cylinder and ridges is defined as 5×10^{-4} m with a high density region around and behind the cylinder with maximum node separation 5×10^{-3} m with transition ratio coarsening parameter of 0.5.

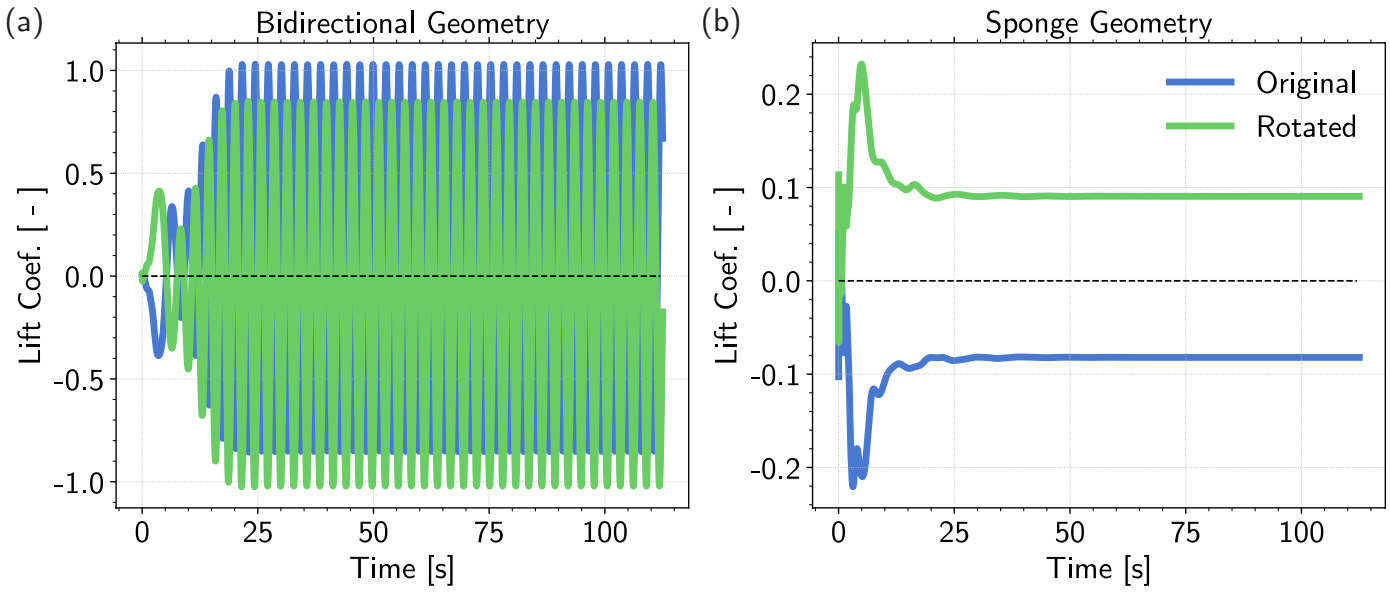

Figure S8: Hydrodynamic analysis: Effect of rotation on lift coefficient. This figure shows the time series of the lift coefficient for geometries in their original configuration with respect to the flow (blue line) and after 180° rotation with respect to the flow direction (green line). Results are shown for (a) *Bidirectional* and (b) *Sponge* ridge designs. The black dashed line shows the $y = 0$ axis of symmetry. Here we see that when the geometry is rotated by 180° the average lift is approximately flipped across the $y = 0$ axis line, demonstrating that the non-symmetric ridge configuration breaks the flow symmetry and biases the lift to a particular direction.

Parameter	Numerical Value
D_{nd}	0.46 mm
D_d	0.23 mm
S	1.34 mm
L	4.56 mm
H	146 mm
R_o	23.5 mm
R_i	21.2 mm

Table S1: Numerical values of geometric parameters used in our simulations.

REFERENCES

[1] Haroutunian, V. (1995). Progress in simulating industrial flows using two-equation models: Can more be achieved with further research? In *NASA Conference Publication*, pages 155–155. NASA.

[2] Blevins, R. D. (1986). Flow-induced vibration. *Rebert E. Kridger Publishing Co.*

[3] Anderson Jr, J. D. (2010). *Fundamentals of aerodynamics*. Tata McGraw-Hill Education.